PLOS ONE

RESEARCH ARTICLE

Solid state characterization and theoretical study of non-linear optical properties of a Fluoro-*N*-Acylhydrazide derivative

Rosemberg F. N. Rodrigues[1,2‡], Leonardo R. Almeida[1,3‡], Florisberto G. dos Santos[2‡], Paulo S. Carvalho, Jr[3☯], Wanderson C. de Souza[1‡], Kleber S. Moreira[1‡], Gilberto L. B. de Aquino[1☯], Clodoaldo Valverde[1,2☯]*, Hamilton B. Napolitano[1☯], Basílio Baseia[4,5☯]

1 Campus de Ciências Exatas e Tecnológicas, Universidade Estadual de Goiás, Anápolis, Goiás, Brazil, **2** Universidade Paulista (UNIP), Goiânia, Goiás, Brazil, **3** Instituto de Física de São Carlos, Universidade de São Paulo, São Carlos, São Paulo, Brazil, **4** Instituto de Física, Universidade Federal de Goiás, Goiânia, Goiás, Brazil, **5** Departamento de Física, Universidade Federal da Paraíba, João Pessoa, Paraíba, Brazil

☯ These authors contributed equally to this work.
‡ These authors also contributed equally to this work.
* valverde@ueg.br

Citation: Rodrigues RFN, Almeida LR, Santos FGd, Carvalho PS, Jr, Souza WCd, Moreira KS, et al. (2017) Solid state characterization and theoretical study of non-linear optical properties of a Fluoro-*N*-Acylhydrazide derivative. PLoS ONE 12(4): e0175859. https://doi.org/10.1371/journal.pone.0175859

Editor: Oksana Ostroverkhova, Oregon State University, UNITED STATES

Received: October 26, 2016

Accepted: March 31, 2017

Published: April 24, 2017

Data Availability Statement: Copies of the crystallographic data can be obtained, free of charge via www.ccdc.cam.ac.uk, under the code CCDC 1489316.

Funding: This work was supported by the Conselho Nacional de Desenvolvimento Científico e Tecnológico (CNPq), Coordenação de Aperfeiçoamento Pessoal de Nível Superior (CAPES), and the Fundação de Apoio à Pesquisa do Estado de Goiás (FAPEG). The funders had no

Abstract

In this work we determine the linear and non-linear optical properties of a Fluoro-*N*-Acylhydrazide derivative (FBHZ), using a combined supermolecule approach and an iterative scheme of electrostatic polarization, where the atoms of neighbouring molecules are represented by point charges. Our results for non-linear optics (NLO) are comparable to those found experimentally, suggesting that FBHZ constitutes an attractive object for future studies and for use as an interesting material for third-order NLO applications. The dynamic electrical properties of FBHZ in different solvent media are reported. Its molecular properties are closely related to supramolecular features; accordingly, we analysed all its crystal structure properties via intermolecular interactions in the solid state, using X-ray crystallography data and Hirshfeld surface (HS), including thermogravimetric analysis (TGA), differential scanning calorimetry (DSC) and hot-stage microscopy (HSM), where the results reveal crystal stability in respect to temperature variation.

Introduction

In recent decades, supramolecular chemistry and the understanding of the linear and non-linear optical properties found in crystal molecular assembly have emerged as an important research topic in the rational design of functional solids[1]. In the solid state context, *N*-Acylhydrazones are important systems to study in view of their conformational versatility and potential applications for polymers and for pharmaceutical, photographic and organic non-linear optic (NLO) materials[2]. Chemically, they represent a class of azomethine compounds, which can easily be obtained by the condensation of aldehydes or ketones and acylhydrazines in the presence of an acid catalyst[3,4]. However, the presence of appropriate substituent groups can modify the distribution of molecular electrons leading to various properties, such

role in study design, data collection and analysis, decision to publish, or preparation of the manuscript.

Competing interests: The authors have declared that no competing interests exist.

as antitumor[5,6], antiviral[7], antimicrobia[8] and vasodilatory[9] activity. As part of our research, we have synthesized (E)-4-(3-fluorobenzyloxy)-N'-benzylidenebenzohydrazide, a fluoro-*N*-Acylhydrazone derivative FBHZ (Fig 1).

NLO has led to a wide range of applications in recent years, including in photonics, opto-electronics, spectroscopy and photon blockades [10–19]. With the evolution of scientific knowledge and new technological advances in optical communication, data processing and storage[20–27], there have been reports of controllable switches with excellent performance in NLO [28]. This has raised great interest among researchers in various fields of knowledge, such as physics, chemistry, engineering, and biology [17–19,29–31]. One of the issues concerns organic materials with a good response, including a response for third-order susceptibility and governed by the second hyperpolarizability. Such materials offer rich and varied behaviour in relation to a second-order NLO process, due to their larger frequency range.

Investigations using varied methods and materials have become important for the application of modern optics [32–34]. As is well known, the NLO properties of a crystal usually come from a material constituted by long asymmetric molecules in such a way that, when crystalized, they organize themselves into a crystalline structure and thus maintain their original asymmetry, to some extent. However, even when working with a crystal formed by small molecules, as in the present case, one can use certain techniques to get a crystal with reasonable nonlinear efficiency. In this line, *ab initio* calculations are employed to obtain the structural properties of the molecule. When organic crystals are involved, one should take into account the effects of neighbouring molecules for a better description of their NLO properties; however, the calculations of these properties require sophisticated theoretical models that robustly represent the electronic properties of a crystalline environment [35–38].

Organic molecules with good NLO properties are of great importance for optical applications; hence, theoretical models to calculate these properties have been developed in recent years, with reasonable results when compared to the experimental values. As an example, we cite a recent work in which the authors used a polarization model to estimate the NLO properties, $\chi^{(1)}$ and $\chi^{(2)}$ of molecular crystals, with significant results when compared with the experimental data [38]. Other embedding schemes have also been designed for molecular crystals [39–43].

In the present work we describe the synthesis and solid-state characterization of an *N*-acylhydrazone derivative, (E)-4-(3-fluorobenzyloxy)-N'-benzylidenebenzohydrazide (FBHZ). From the Single Crystal X-ray Diffraction (SCXRD) analysis, a detailed inspection of molecular assembly reveals the presence of C–H···O, N–H···O, C–H···π (localized) and C–H···F contacts in the FBHZ structure. Here we also present an *ab initio* study using a supermolecule approach to polarization to calculate the dipole moment (μ), the linear polarizability (α), the first hyperpolarizability (β) and second hyperpolarizability (γ) for the FBHZ, exhibiting NLO properties.

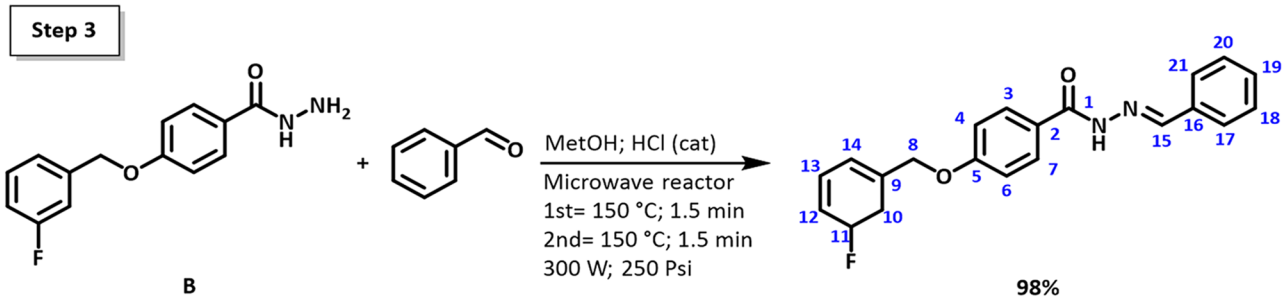

Fig 1. Synthesis of (E)-N'-benzylidene-4-((3-fluorobenzyl)oxy)benzohydrazide (C21H17FN2O2) (FBHZ).

https://doi.org/10.1371/journal.pone.0175859.g001

Experimental and computational procedures

Synthesis

FBHZ was synthesized by a three-step reaction: **Step 1** synthesis of the compound methyl 4-[(3-fluorobenzyl)oxy]benzoate (**A**); S**tep 2** synthesis of the compound 4-[(3-fluorobenzyl)oxy] benzohydrazide (**B**) (Steps 1 and 2 see S1 Fig). (Fig 1) shows the **Step 3** synthesis of the compound (E)-4-(3-fluorobenzyloxy)-N'-benzylidenebenzohydrazide (FBHZ): **B** (0.260g, 1.0 mmol) was dissolved in methanol (2 mL), followed by addition of 3-fluorbenzaldehyde (1.0 mmol) and a single drop of hydrochloric acid (HCl 37%). The mixture was heated for two cycles of 1.5min at 150˚C in a microwave reactor. The reaction was monitored by Thin-layer chromatography (TLC) and, after verifying product formation, the reaction was cooled and the solvent removed by using the vacuum rotary evaporation system. Yield 98%. Molecular formula: C21H17FN2O2 (348.38 g.mol^{-1}).

Single crystal X-ray analysis

The single-crystal X-ray diffraction data for FBHZ were collected at 296(2) K using an APEX2 [44] diffractometer with MoKα radiation (λ = 0.71073 Å). The cell refinement and data reduction were carried out also using the software SAINT[45]. The structure was solved by direct methods using SHELXS-2013[46] and anisotropically refined with full-matrix least-squares on F^2 using SHELXL.[47] The hydrogen atoms on the carbon atoms were positioned geometrically and refined through the riding model [C-H(aromatic) = 0.93 Å with Uiso(H) = 1.2Ueq (C); C-H_2 = 0.98 Å, with Uiso(H) = 1.2 Ueq(C); N-H = 0.86 (0.92) Å, with Uiso(H) = 1.2 Ueq (N)]. Molecular representation, tables and pictures were generated by Olex2,[48] ORTEP-3 [49] and Mercury (version 3.8)[50,51] programs. The UNI intermolecular potential force field (FF)[52,53] was carried out by using via Mercury (version 3.8),[50,51] providing information about energies of strongest lattice contributions coming from inter-contacts. Possible hydrogen bonds were evaluated by using the PARST routine[54] and through the supramolecular features in crystal packing[55–59]. Crystallographic information files were deposited in the Cambridge Structural Data Base[60] under the code CCDC 1497913. Copies of the data can be obtained, free of charge, via www.ccdc.cam.ac.uk.

Hirshfeld surface analysis

The Hirshfeld surface (HS) and its associated 2D fingerprint plot were performed using Crystal Explorer 3.1[61,62] by constraining these calculations in Density Functional Theory (DFT) at level Becke88/LYP/6-311G(d,p) to experimental X-ray diffraction data (from single crystal FBHZ) via Tonto.[63,64] The surface was generated on the basis of the normalized contact distances, which are defined in terms of d_i (the distance to the nearest nucleus within the surface) and d_e (the distance from the point to the nearest nucleus external to the surface) relative to van der Waals radii[65,66] of the atoms. The high resolution default of d_{norm} surface (volume: 424.80 Å^3 and area: 399.79 Å^2) was mapped over the colour scale, ranging from −0.369 (red) to 1.201 Å (blue), with the fingerprint plots using the expanded 0.6–2.8 Å view of d_e *vs.* d_i.

Thermal analysis

Hot-stage microscopy was performed on a Leica DM2500P microscope connected to the Linkam T95-PE hot-stage equipment. Data were visualized with the Linksys 32 software for hot-stage control. The crystals of FBHZ were placed on a 13mm glass coverslip and put on a 22mm-diameter pure silver heating block inside the stage. The sample was heated at a ramp rate of 10˚C.min^{-1} up to a final temperature of 195˚C, but discontinued when all material

melted. Thermogravimetric analyses (TGA) were evaluated by using a NETZSCH TG 209F1, at a heating rate of 10˚C.min^{-1}, under nitrogen atmosphere and at a temperature range of 25 to 400˚C. The Differential Scanning Calorimetric (DSC) measurements were carried out in a NETZSCH DSC 204 at a temperature range of 25 to 400˚C and a heating rate of 10˚C.min^{-1} under nitrogen atmosphere, using 2.040 mg of sample mass.

Theoretical calculations

In this work, we took advantage of a supermolecule approach that allows us to analyse the polarization effects of the environment on the electrical properties of FBHZ. In this method, the atoms of surrounding molecules are seen as point charges, as shown in (Fig 2), in which each FBHZ molecule (ball and stick) is surrounded by other equal units (wireframe). For the FBHZ a set of 9×9×9 unit cell was used, with 2 asymmetric units in each unit cell, totalizing 1458 unit cells with 62694 atoms, 43 of them forming the FBHZ molecule (Fig 3) to be engaged by the rest. The atoms that form the molecules that surround the FBHZ isolated are treated as point charges, since the interactions between molecules have a dominant electrostatic nature, taking into account long-range electrostatic effects [67,68]. Using the iterative process in which the electrical polarization effects are considered, we have as a major goal the determination of the linear and nonlinear electrical properties of the isolated and embedded FBHZ forming the crystal.

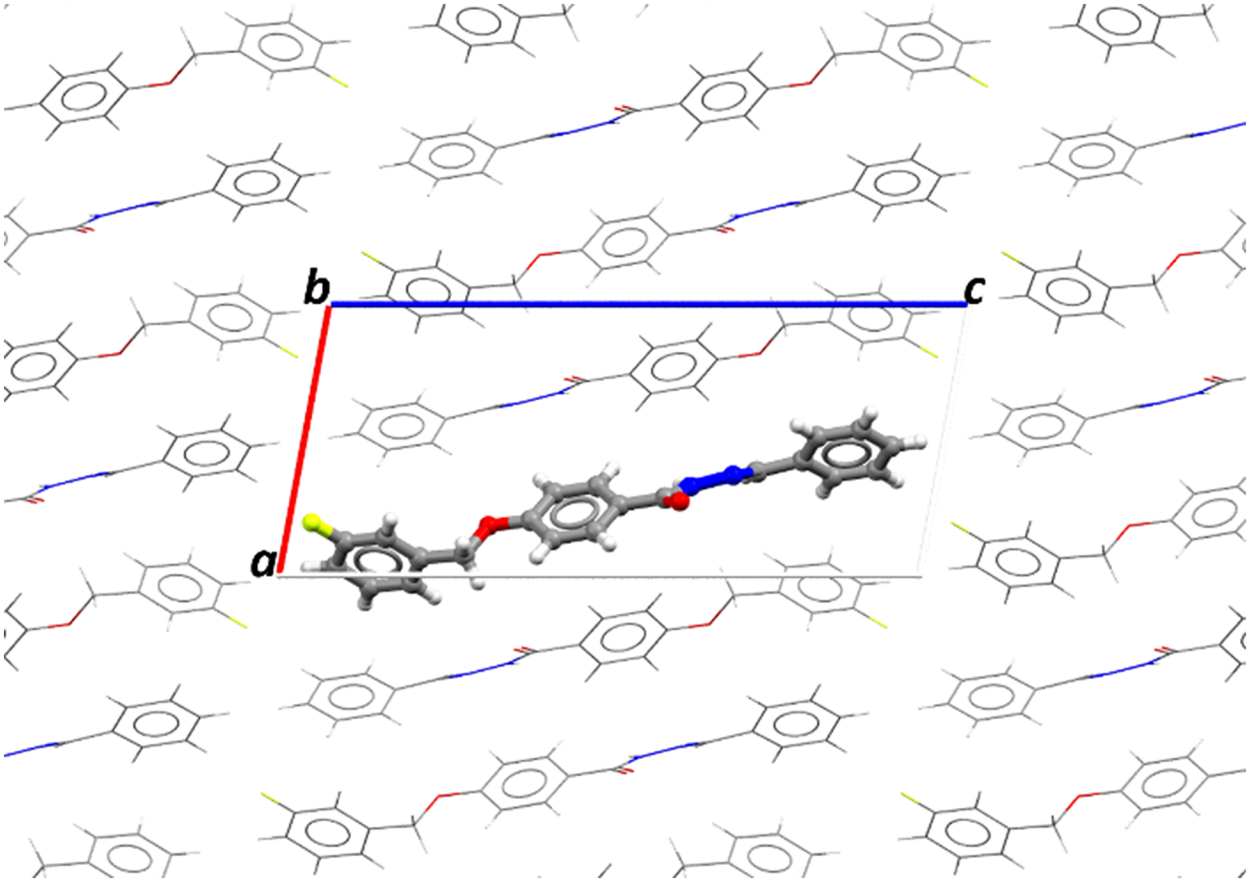

Fig 2. Projection along axis b of the crystal showing the asymmetric unit of embedded FBHZ in the polarization field, the atoms of the molecules of the involved units being treated as point charges.

https://doi.org/10.1371/journal.pone.0175859.g002

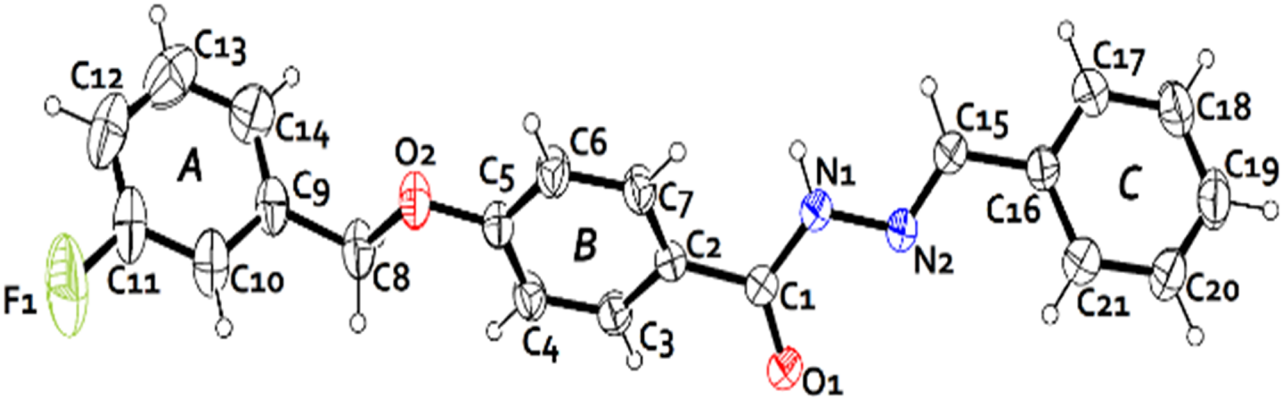

Fig 3. The molecular structure of the FBHZ showing the atom-labelling scheme. Thermal ellipsoids drawn at the 30% probability level. The hydrogen atoms are shown as arbitrary spheres.

https://doi.org/10.1371/journal.pone.0175859.g003

To this end, we started (step zero) with the isolated molecule, via a fit of the electrostatic potential (ChelpG) obtained from the 6–311+G(d) basis set at the MP2 level, described by its charge distribution in a vacuum. Then (i) we calculated the partial atomic charges (ChelpG) for a single isolated molecule of the asymmetric unit; (ii) in the position of each corresponding atom in the generated unit cells, we replaced the atom with its partial atomic charge obtained in item (i); (iii) we calculated the static electric properties (dipole moment and second hyper-polarizability), as well as the new partial atomic charges of the asymmetric unit; (iv) we returned to item (ii) and repeated the procedure until convergence in the electric molecular properties is achieved, as implemented in previous works using this method [36–38].

These calculations showed that a set of 5x5x5 unit cells guarantees fast convergence of the dipole moment of the crystal, so we used a larger arrangement (9x9x9) to ensure a stable value of the dipole moment. The Gaussian-09 program was used in all calculations.

The numerical evaluation employs the following definitions, e.g., the total dipole moment μ,

$$\mu = \sqrt{\mu_x^2 + \mu_y^2 + \mu_z^2}\,, \tag{1}$$

the linear average polarizability $\langle\alpha\rangle$,

$$\langle\alpha\rangle = \frac{1}{3}\sum\nolimits_{i=1}^{3} \alpha_{ii}, \tag{2}$$

the total intrinsic first hyperpolarizability β_{Tot} defined as

$$\beta_{Tot} = \sqrt{(\beta_x^2 + \beta_y^2 + \beta_z^2)}, \tag{3}$$

where

$$\beta_i = \frac{1}{3}\sum\nolimits_j (\beta_{ijj} + \beta_{jij} + \beta_{jji}). \tag{4}$$

The experimentally relevant quantity is

$$\beta_{||} = \frac{1}{5}\sum\nolimits_{i=1}^{3} (\beta_{zii} + \beta_{izi} + \beta_{iiz}), \tag{5}$$

where z is oriented in the direction of the dipole moment of molecule. Sometimes the

equivalent quantity $\beta_{vec} = \frac{5}{3}\beta_{||}$ is used. The second average hyperpolarizability [69], is given by

$$\langle\gamma\rangle = \frac{1}{15}\sum_{ij=x,y,z}(\gamma_{iijj} + \gamma_{ijij} + \gamma_{ijji}). \quad (6)$$

The macroscopic linear parameter $\chi^{(1)}$, second-order nonlinear $\chi^{(2)}$ and third-order nonlinear susceptibilities $\chi^{(3)}$ of the crystals can be estimated in a first approximation via the following relations,

$$\chi_{ij}^{(1)} = \frac{\alpha_{ij}}{V}, \quad (7)$$

$$\chi_{ijk}^{(2)} = \frac{\beta_{ijk}}{2V}, \quad (8)$$

and,

$$\chi^{(3)} = \frac{N}{V}\langle\gamma\rangle, \quad (9)$$

where N stands for the number of atoms in the unit cell, and V represents its volume Table 1; the dipole moment Table 2; the components α_{ij} (i, j stand for x, y, z) of the linear polarizability are given in Table 3; ε_0 is the vacuum permittivity and it was built into the Eqs (10), (11) and

Table 1. Crystallographic information on the FBHZ.

Identification code	CCDC 1497913	
Empirical formula	$C_{21}H_{17}FN_2O_2$	
Formula weight	348.36	
Temperature (K)	296(2)	
Crystal system	Monoclinic	
Space group	$P2_1$	
Unit cell dimensions	a = 8.5766(5) Å	α = 90°
	b = 5.1893(3) Å	β = 100.451(2)°
	c = 19.7867(10) Å	γ = 90°
Volume (Å^3)	866.03(8)	
Z	2	
ρ_{calc} (g/cm^3)	1.336	
μ/mm^{-1}	0.774	
F(000)	364.0	
Crystal size (mm^3)	0.1 × 0.1 × 0.1	
Radiation	CuKα (λ = 1.54184)	
2Θ range for data collection (°)	9.09 to 136.902	
Index ranges	$-10 \leq h \leq 10$, $-6 \leq k \leq 5$, $-23 \leq l \leq 23$	
Reflections collected	10407	
Independent reflections	3088 [R_{int} = 0.0436, R_{sigma} = 0.036]	
Data/restraints/parameters	3088/1/236	
Goodness-of-fit on F^2	1.046	
Final R indexes [I> = 2σ (I)]	R_1 = 0.0388, wR_2 = 0.1071	
Final R indexes [all data]	R_1 = 0.0502, wR_2 = 0.1117	
Largest diff. peak/hole (e Å^{-3})	0.18/-0.21	
Flack parameter	0.13(9)	

https://doi.org/10.1371/journal.pone.0175859.t001

Table 2. MP2/6-311+G(d) results for the components of the dipole moment (D) as function of the iterative process.

FBHZ	μ_x	μ_y	μ_z	μ
Isolated	1.67	4.73	-0.15	5.02
Embedded	1.95	3.89	-0.43	4.37
Δ%	16.77	17.76	186.67	12.95

https://doi.org/10.1371/journal.pone.0175859.t002

Table 3. MP2/6-311+G(d) results for the linear polarizability (10^{-24}) esu).

FBHZ	α_{xx}	α_{xy}	α_{yy}	α_{xz}	α_{yz}	α_{zz}	$\bar{\alpha}$
Isolated	28.76	1.17	30.59	−11.97	1.07	55.54	38.30
Embedded	28.83	1.01	30.66	−12.15	1.27	55.93	38.47
Δ%	0.24	13.68	0.23	1.50	18.69	0.70	0.44

https://doi.org/10.1371/journal.pone.0175859.t003

(12), the components β_{ijk} of the first hyperpolarizability are given in Table 4, with i, j, k, standing for x, y, z. The values of $\langle\gamma\rangle$ for the isolated and embedded molecules are given in Table 5. The conversion of unit between $\chi^{(n)}$ and α, β and γ are made based on the following relationships,

$$\chi^{(1)}[SI] = 4\pi\chi^{(1)}[esu], \quad and \ \alpha[SI] = 4\pi \times 10^{-6}\,\alpha[esu], \tag{10}$$

$$\chi^{(2)}\left[\frac{m}{V}, SI\right] = \frac{4\pi \times 10^{-4}}{3}\chi^{(2)}[esu], \quad and \ \beta\left[\frac{m^4}{V}, SI\right] = \frac{4\pi \times 10^{-10}}{3}\beta[esu], \tag{11}$$

and,

$$\chi^{(3)}\left[\frac{m^2}{V^2}, SI\right] = \frac{4\pi \times 10^{-8}}{9}\chi^{(3)}[esu], \quad and \ \gamma\left[\frac{m^5}{V^2}, SI\right] = \frac{4\pi \times 10^{-14}}{9}\gamma[esu]. \tag{12}$$

Table 4. MP2/6-311+G(d) results for the first hyperpolarizability (10^{-30} esu).

	Isolated	Embedded	Δ%
β_{xxx}	0.21	-0.15	171.43
β_{xxy}	-0.25	-0.09	64.00
β_{xyy}	0.20	-0.02	110.00
β_{yyy}	0.56	2.02	260.71
β_{xxz}	1.29	1.49	15.50
β_{xyz}	0.99	1.13	14.14
β_{yyz}	-0.47	-0.31	34.04
β_{xzz}	-2.64	-3.16	19.70
β_{yzz}	-1.60	-1.54	3.75
β_{zzz}	9.85	11.00	11.68
β_{Tot}	10.98	12.64	15.12

https://doi.org/10.1371/journal.pone.0175859.t004

Table 5. Linear optical susceptibility tensor components $\chi^{(1)}$ of FBHZ.

FBHZ	$\chi^{(1)}_{xx}$	$\chi^{(1)}_{xy}$	$\chi^{(1)}_{yy}$	$\chi^{(1)}_{xz}$	$\chi^{(1)}_{yz}$	$\chi^{(1)}_{zz}$
	0.42	0.01	0.44	−0.18	0.02	0.81

https://doi.org/10.1371/journal.pone.0175859.t005

Results and discussion

Synthesis and spectroscopic characterization

The FBHZ was synthesized by the condensation reaction [3], following the three-step reaction herein described. Solid obtained characteristics: yield 98%; molecular formula $C_{21}H_{17}FN_2O_2$ (348.38 g.mol^{-1}); light beige colour; melting point 193–195˚C. Single crystals (plates) of FBHZ suitable for X-ray diffraction studies were obtained by slow evaporation from acetone solution at room temperature (~25˚C). ^{1}H NMR (500 MHz, DMSO-d6) δ: 5.23 (s, 2H – 8) 7.15 (m, 3H–12, 6 and 4) 7.32 (d, 2H–14 and 10) 7.45 (m, 4H–13, 18, 19 and 20) 7.72 (d, 2H–17 and 21) 7.91 (d, 2H–7 and 3) 8.45 (s, 1H–15) 11.74 (s, 1H –NH) (S4 Fig). ^{13}C NMR (125 MHz, DMSO-6d) δ: 99.67 (C-8) 105.77 (C-12, C-10, C-6 and C-4) 107.35 (C-14) 107.99 (C-2) 109.26 (C-17 and C-21) 111.93 (C-18 and C-21) 115.20 (C-3 and C-7) 115.72 (C-13) 121.92 (C-19) 122.13 (C-16) 122.41 (C-9) 134.80 (C-15) 135.07 (C-11) 143.58 (C-1) 151.69 (C-5) (S5 Fig). IR (4000–400 cm^{-1}): (C-O) 1183 and 1251; (C-F) 1363; (C = N) 1532; (C = O) 1642; (N-H); 3254 (S2 Fig). MS (m/z): [M+] 348; Fragments: 239; 229; 119; 109 (S3 Fig). Maximum absorbance of 0.805Abs at λ = 302nm on UV scan with 3.2.10^{-2}mg.mL^{-1} of sample in ethanol 99.9% (S6 Fig).

Solid state characterization

The characterization of FBHZ was performed using SCXRD and thermal analysis. The compound crystallizes in the non-centrosymmetric space group $P2_1$ with a single molecule in the asymmetric unit (ASU) (Z' = 1) (Fig 3). The crystal packing of FBHZ is shown in (Fig 4) and the crystal data are given in Table 1.

Additional crystallographic information is present in S6 Fig and S1–S5 Tables. Conformational features were noted through angles (∠, ˚) between planes and fragment dihedral angles (τ, ˚) for the FBHZ, which assumes a non-planar geometry from all three aromatic ring planes: ∠A–B = 75.57˚ [τ(*C5–O2–C8–C9*) = -175.97(4˚]; ∠B–C = 69.05˚ [τ(*C16–C15–N2–N1*) = -179.39(8˚, τ(*O1–C1–N1–N2*) = -4.76(5˚, τ(*C1–N1–N2–C15*) = 168.67(8˚ and τ(*C2–C1–N1–N2*) = 174.59(8˚] and ∠A–C = 12.54˚.

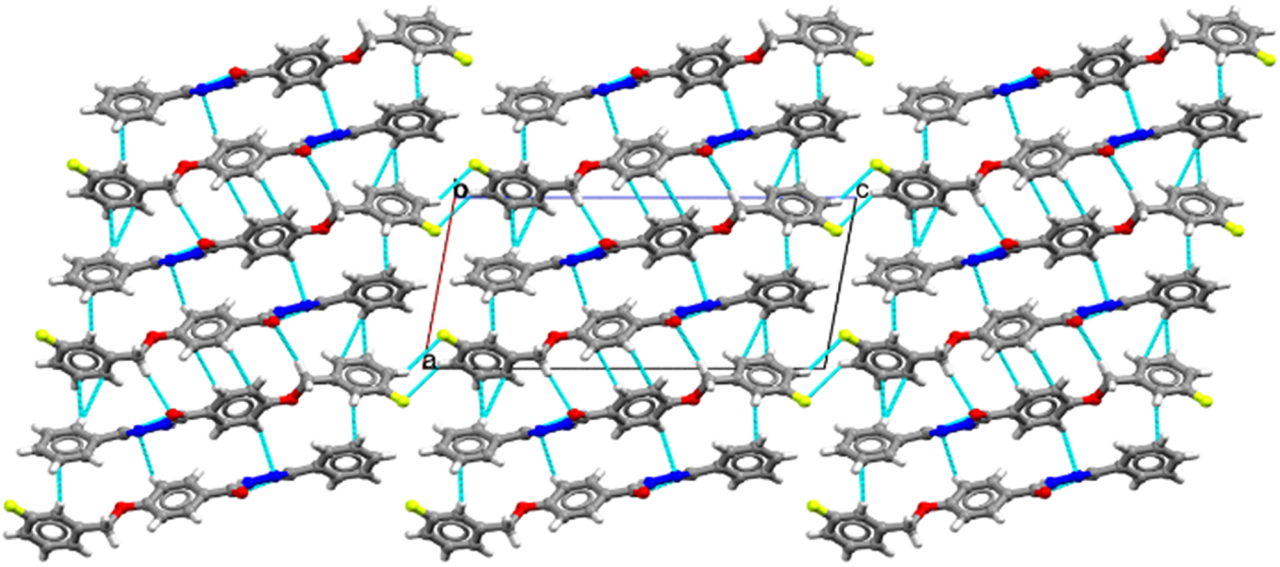

Fig 4. Crystal packing diagram of FBHZ. Cyan dashed lines indicate all possible contacts.

https://doi.org/10.1371/journal.pone.0175859.g004

Further support for the interactions in the supramolecular arrangement comes from values calculated by the UNI intermolecular potential force field (FF) approach,[52,53] as implemented in Mercury (version 3.8).[50,51] The graphical view of the results (Fig 5a) underlines the fact that the three strongest lattice contributions are between ASU (mol 0) and each of the molecules in the crystal packing (mol 1, mol 2 and mol 3). Inter-fragment energies[70,71] are: -55.4 kJ.mol^{-1} [mol 0 to mol 1 –screw (2-fold)], -55.3. kJ.mol^{-1} [mol 0 to mol 2 –screw (2-fold)] and -53.8 kJ.mol^{-1} [mol 0 to mol 3 –translation]. These calculations also provide the total packing energy (-199.6 kJ.mol^{-1}).

In the crystal structure, a $C_2^1(6)$ motif is formed by the C15–H15···O1 [$d_{C15\cdots O1}$ = 3.374(4) Å] and N1–H1···O1 [$d_{N1\cdots O1}$ = 3.057(3) Å] hydrogen bonds. As a consequence, molecules are arranged into a 1D-chain along the [10] direction (Fig 5b). Adjacent chains are 2D assembled (Fig 5c) by the formation of the C17–H17···π (π localized on C13 and C14) [$d_{C17\cdots C13}$ = 3.654(5) Å; $d_{C17\cdots C14}$ = 3.722(5) Å], C3–H3···π (π localized on C4) [$d_{C3\cdots C4}$ = 3.770(5) Å], C8–H8B···O1 [$d_{C8\cdots O1}$ = 3.576(4) Å], C6–H6···N2 [$d_{C6\cdots N2}$ = 3.545(4) Å], C10–H10···π (π localized on C20) [$d_{C10\cdots C20}$ = 3.633(5) Å] weak hydrogen bonds[56,58,72–76]. The 3D assembly is completed considering a weak hydrogen bond C–H···F[77–80] between C12–H12···F1 [$d_{C12\cdots F1}$ = 3.477(6) Å], which holds together the molecules along the [1] direction (Fig 5d), and the existence of these combined interactions supports the supramolecular assembly.

Hirshfeld Surface (HS) analysis was performed to identify important intermolecular interactions and their quantitative contributions to the stability of the supramolecular assembly of FBHZ. Furthermore, the analysis confirms the existence of weak interactions disclosed by computational methods. The (Fig 6a and 6b) presents the d_{norm} maps of FBHZ with interaction areas (red) located on the O-atom of carbonyl (C = O), H-atoms of aromatic (C-H) π-localized and N-atoms of the (HN-N = C) azo group. These red spots observed corroborate the regions of contact in the supramolecular arrangement.

The associated d_e *vs.* d_i fingerprint plots summarize the contributions of intermolecular contacts to the total HS area of FBHZ (Fig 7). The two peaks at 1.4–1.2 Å d_i+d_e are associated with O···H contacts (12.4%) and attributed to C–H···O/N–H···O interactions of the 1D and 2D assembly of FBHZ. There is evidence of C–H···π (localized) contacts in the structure associated with H···C contacts (36.9%), the largest value from this HS area, which occur as a characteristic peak on the side borders of the plot at 1.5–2.6 Å d_i+d_e. These contacts happen around the hydrophobic region, in this case in aromatic groups.

The HS analysis of FBHZ molecules shows the second largest contribution from H···H type contacts, contributing to 32.5% of the total area. This is in accordance with the strong contribution of aromatic groups to the formation of hydrophobic regions where various *van der* Waals contacts are formed. Noticeable contributions from H···F and N···H contacts are also observed, showing a percentage of 9.9% and 6.4% of HS area, respectively. H···F is associated with C–H···F and N···H to C–H···N weak hydrogen bonds, as previously discussed.

In order to characterize the crystalline structure of FBHZ fully, DSC/TGA and Hot-stage Microscopy analysis were performed, and the results are presented in (Fig 8). The DSC measurement shows only one endothermic event centred at 190.47˚C. The TGA curve shows the beginning of weight loss at 224˚C. Since no weight loss is detected in the TGA curve until ~220˚C, the endothermic event is associated with a solid-liquid phase transition. This transformation is irreversible, since no corresponding event occurs during the cooling-reheating cycles of DSC, and meanwhile the entropy decrease due to the ordering of FBHZ molecules on crystalline state within the system is overcompensated by the thermal randomization of the surroundings. Furthermore, the event at 190.47˚C in the DSC curve

corresponds to the complete melting of the sample and was confirmed by the Hot-stage Microscopy analysis, which takes close values as in the range 182–198˚C. No habit or colour changes are observed for the sample between 22 and 152˚C. However, the solid-liquid phase transformation is detected in Hot-stage photography, when the crystals change their colour,

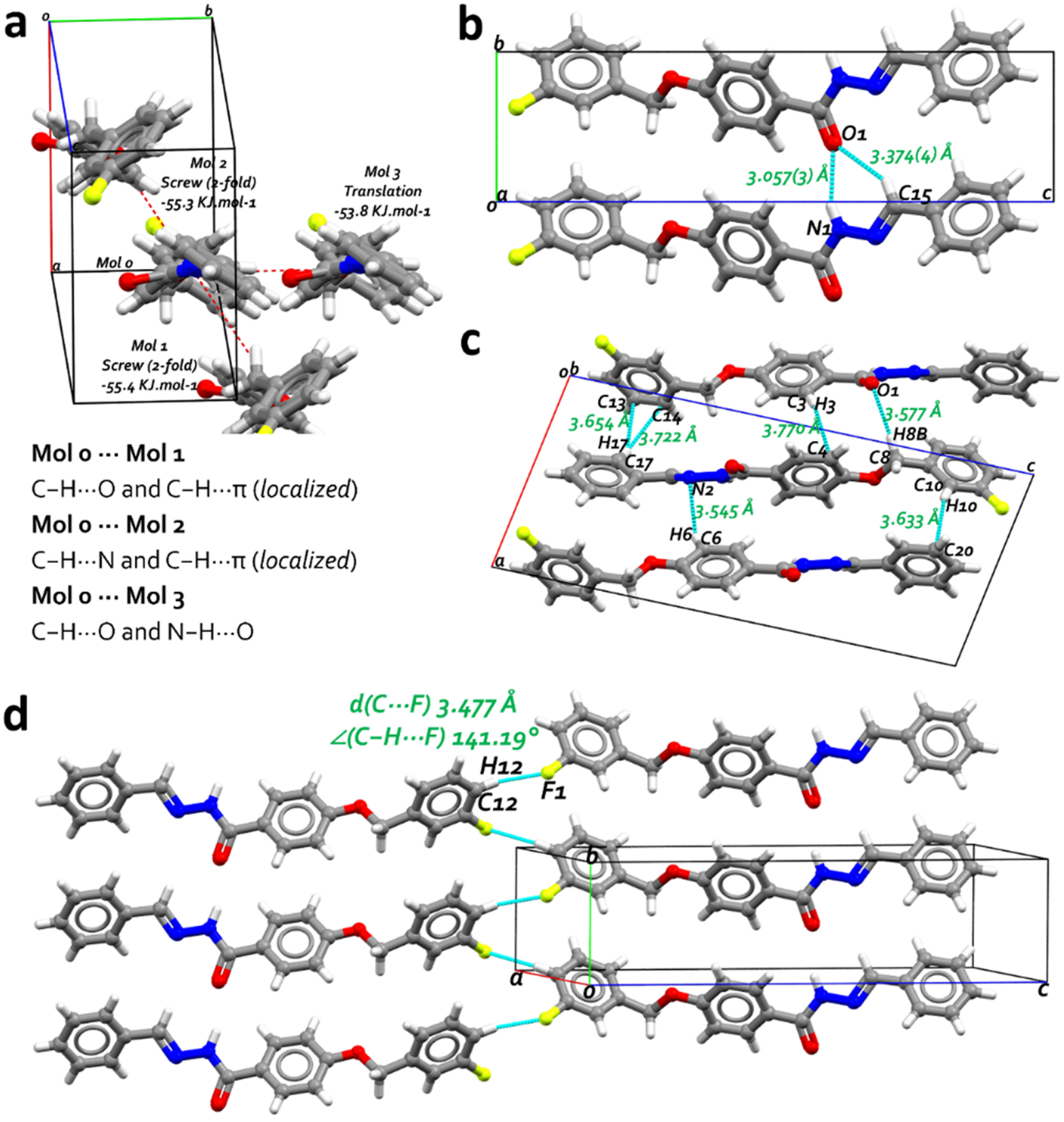

Fig 5. a) UNI intermolecular potential calculation results, showing the three largest lattice contributions of FBHZ in red dashed lines from molecule 0 to each independent molecule [Mol 1: -55.4 kJ.mol-1; Mol 2: -55.3 kJ.mol-1; and Mol 3: -53.8 kJ.mol-1]. b) Bifurcated C−H···O/N−H···O hydrogen bonds with donor-acceptor distances [d(D···A) Å]. c) weak hydrogen bonds C−H···O/N−H···O and C−H···π (localized) contacts with donor-acceptor distances [d(D···A) Å]. d) The non-conventional C−H···F hydrogen bonds with donor-acceptor distances [d(D···A) Å] and C−H···F angles [∠(C−H···F) ˚].

https://doi.org/10.1371/journal.pone.0175859.g005

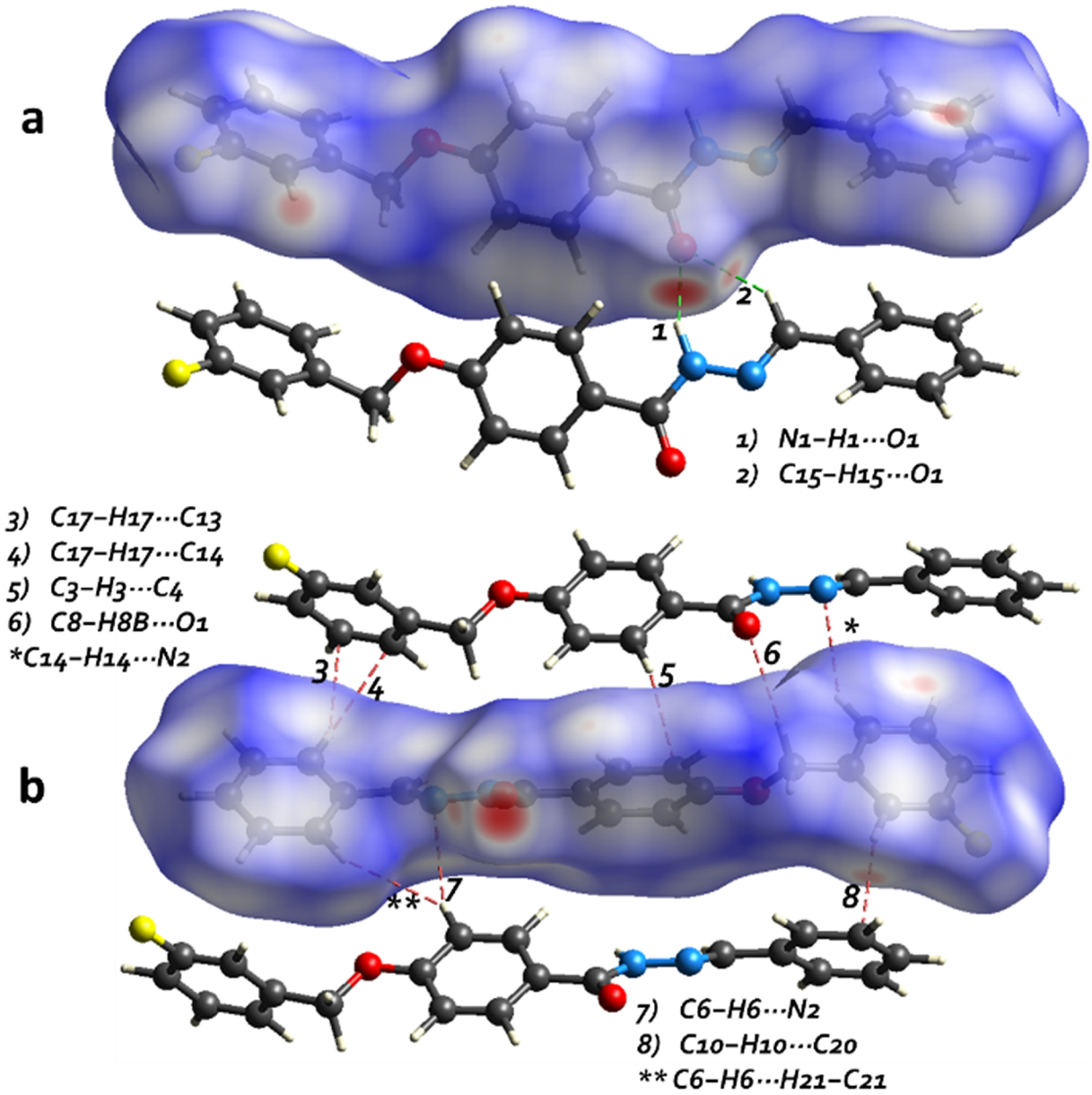

Fig 6. The HS mapped with dnorm property, highlighting regions of contact such as H···O (C–H···O/N–H···O hydrogen bonds), H···N (C–H···N weak hydrogen bonds) and H···C [C–H···π (localized on C)] contacts.

https://doi.org/10.1371/journal.pone.0175859.g006

becoming an opaque material at ~190˚C. The complete melting of the sample is achieved at 194˚C.

Theoretical study of NLO properties

We addressed the evolution of the electrical properties of dipole moment (μ), linear polarizability (α), first hyperpolarizability (β) and second hyperpolarizability (γ). We took into account the number of iterations for FBHZ, both isolated and embedded by other molecules in the same structure. The MP2 theory levels were used with the basis set of functions 6–311 +G(d) for all electrical properties, with the exception of the second hyperpolarizability, in

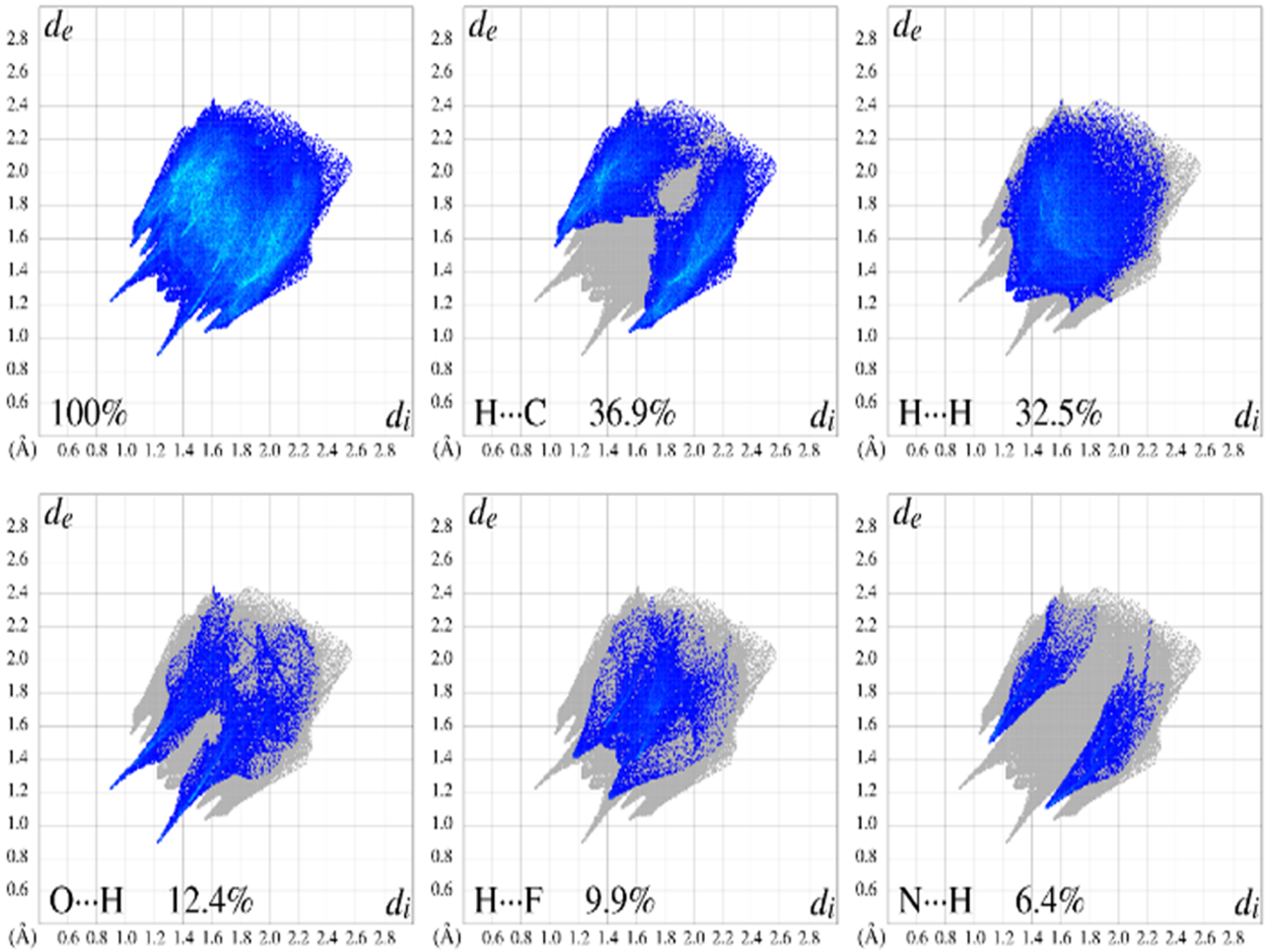

Fig 7. 2D fingerprint plots showing the percentage decomposition from each indicatory type of contact related to C–H···π [H···C 36.9%], C–H···O [O···H 12.4%], C–H···F [H···F 9.9%], N–H···O [N···H 6.4%] and H···H 32.5% in HS for FBHZ.

https://doi.org/10.1371/journal.pone.0175859.g007

which the CAM-B3LYP was used, albeit keeping the same basis set functions. Previous studies have shown that the set basis used in this work is recognized as adoptable, [36] since the results for the dipole moment are reasonable in comparison with experimental data [81]. The following tables show the results of these properties of the crystal as a function of the iteration numbers.

The applicability of the supermolecule approach and the scheme of electrostatic polarization is advantageous due to the rapid convergence of the dipole moment of FBHZ throughout the process, in which six iterations were considered. The convergence of iterative series for this electrical property can be seen in (Fig 9). The value of the total dipole moment ($\boldsymbol{\mu}$) for the embedded FBHZ is 4.37 D, showing a decrease of 12.95% when compared with the isolated FBHZ, 5.02 D. Equivalent results for the dipole moment due to crystal field effects have also been reported [37,82,83]. In Table 2, the $\boldsymbol{\mu}_y$ component is shown displaying values closer to the final result, hence providing the greatest contribution to the dipole moment. On the other hand, the $\boldsymbol{\mu}_z$ is the component that provides the least contribution.

The present supermolecule approach, combined with an electrostatic polarization scheme, satisfactorily reproduces the average value of the linear polarizability when compared with experimental results [38]. The calculations of the linear polarizability, shown in Table 3, were

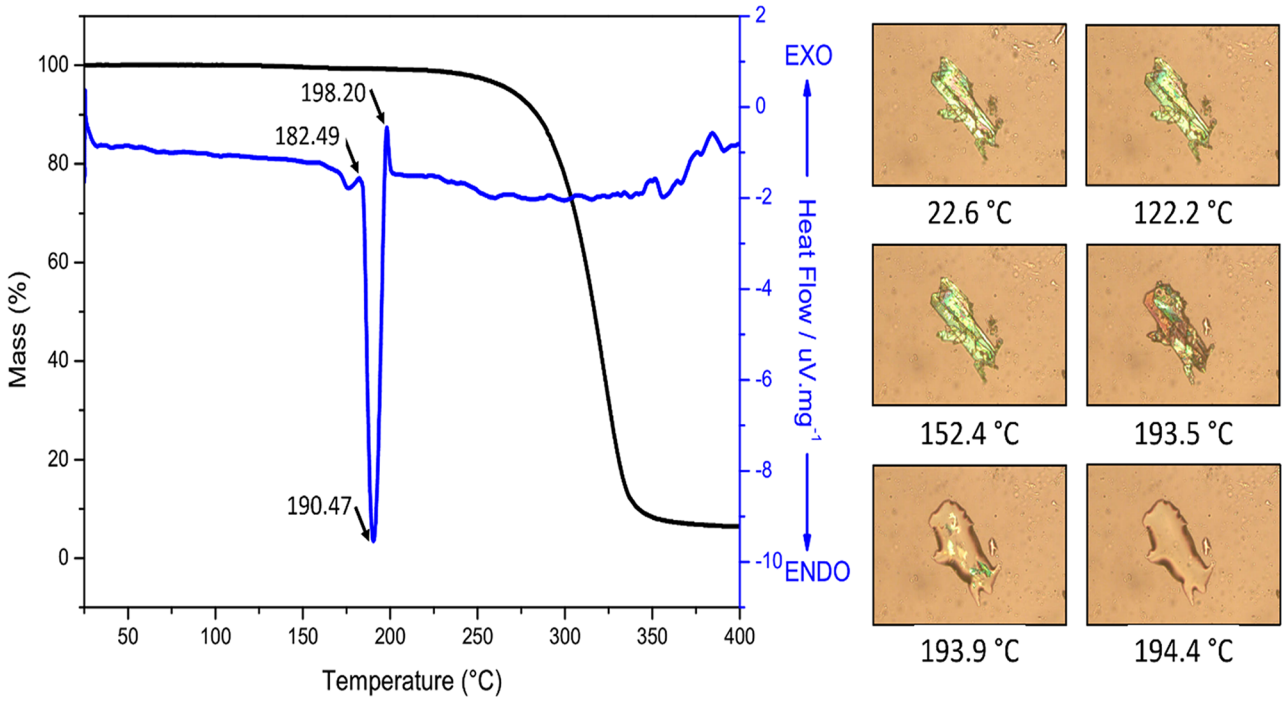

Fig 8. Heating-cooling-reheating DSC and TGA data for the FBHZ. The solid-liquid transition via Hot-stage Microscopy analysis is also shown.

https://doi.org/10.1371/journal.pone.0175859.g008

implemented via MP2 using the base function set 6–311+G(d). Analysing the second linear property, we note that the value of the linear polarizability $\langle\alpha\rangle$ for the isolated FBHZ is 38.30×10^{-24} esu, whereas for the embedded molecule one finds 38.47×10^{-24} esu, showing an increase of 0.44%. Checking the components, we notice them exhibiting different variations, in which $\boldsymbol{\alpha_{xx}}$, $\boldsymbol{\alpha_{yy}}$, $\boldsymbol{\alpha_{yz}}$, $\boldsymbol{\alpha_{zz}}$ show a percentage increase, with the component $\boldsymbol{\alpha_{yz}}$ exhibiting the greatest variation, 18.69%. On the other hand, the $\boldsymbol{\alpha_{xy}}$ is reduced in percentage by 13.68%.

The same method as that applied in the foregoing paragraph also satisfactorily reproduces the value of the first hyperpolarizability in comparison with experimental results [38]. The calculations of the first hyperpolarizability were implemented with the MP2 method, using the base function set 6–311+G(d). Considering now the first nonlinear property, Table 4 shows the first hyperpolarizability values for FBHZ, and the value for the (β_{Tot}) is 10.98×10^{-30} esu isolated and 12.64×10^{-30} esu embedded, corresponding to an increase of 15.12%. Higher percentages also occur, as found in the $\boldsymbol{\beta_{xxx}}$ 171.43% and $\boldsymbol{\beta_{xyy}}$ 110% components, in which reduction occurs; on the other hand, one finds the components $\boldsymbol{\beta_{xxy}}$ and $\boldsymbol{\beta_{yyy}}$ with 64% and 260.71%, respectively, reporting a percentage increase. The other components also undergo variations due to influences that come from polarization of the environment; but in this case the magnitude is reduced, as happens for $\boldsymbol{\beta_{Tot}}$. We also observed component $\boldsymbol{\beta_{zzz}}$ giving the greatest contribution to the first total hyperpolarizability, ranging in 14.91% (embedded). The first calculated hyperpolarizability of the crystal FBHZ is better than the experimental result for the (1E,4E)-1,5-di-p-tolylpenta-1,4-dien-3-one; our result is 40% higher and becomes an attractive object for future studies in nonlinear optics [84].

The use of the supermolecule approach generally leads to a better description of the Optical Properties. The calculated values $\chi^{(1)}$ and $\chi^{(2)}$ are summarized in Tables 5 and 6.

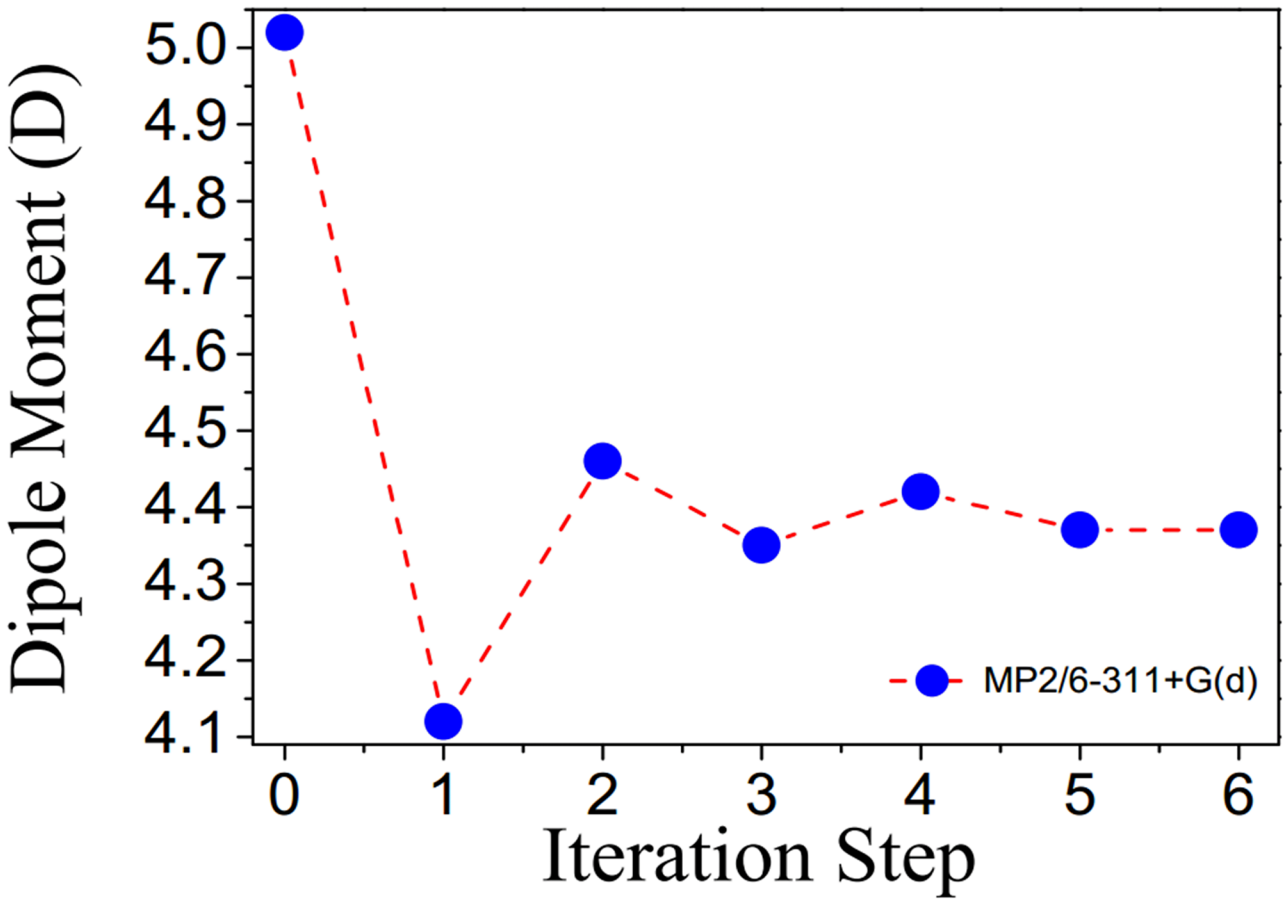

Fig 9. Evolution of values of the dipole moment of the FBHZ with the respective iteration numbers. A 9×9×9 unit cell assembly was considered (step 0 indicates the isolated molecule and the other steps indicate the embedded molecule).

https://doi.org/10.1371/journal.pone.0175859.g009

Table 7 displays the second hyperpolarizability ⟨γ⟩ in the static case; it presents the value 65.63×10^{-36} esu for the isolated FBHZ, while the embedded FBHZ shows a slight increase of 5.12% to the value of 68.99×10^{-36} esu. A. N. Castro et al. [37] explained how to increase this percentage, due to the influence of an electrostatic field. Observing all components, we notice they undergo a slight increase in their value, with the exception of the γ_{xxxx} component, which undergoes a reduction of 3.87%. For the embedded FBHZ, there are N = 86 atoms inside the unit cell and the cell volume V = 866.03 Å^3; we have found $\chi^{(3)} \approx 10^{-19}\ m^2/V^2$ (*SI*). This result has the same order of magnitude of the value found for bulk gold[85,86], indicating the reasonability of our result. This demonstrates that FBHZ constitutes a promising object for applications in quantum dots[87].

Accordingly, the percentage differences are more significant for the first hyperpolarizability compared to the linear polarizability and second hyperpolarizability. This happens because the polarization effects of the crystalline environment have a greater impact on the components of

Table 6. Second-order nonlinear optical susceptibility tensor components $\chi^{(2)}$ (in pm/V) of FBHZ.

FBHZ	$\chi^{(2)}_{xxx}$	$\chi^{(2)}_{xxy}$	$\chi^{(2)}_{xyy}$	$\chi^{(2)}_{yyy}$	$\chi^{(2)}_{xxz}$	$\chi^{(2)}_{xyz}$	$\chi^{(2)}_{yyz}$	$\chi^{(2)}_{xzz}$	$\chi^{(2)}_{yzz}$	$\chi^{(2)}_{zzz}$
	−0.04	−0.02	−0.01	0.49	0.36	0.27	−0.08	−0.76	−0.37	2.66

https://doi.org/10.1371/journal.pone.0175859.t006

Table 7. CAM-B3LYP/6-311+G(d) results for the second hyperpolarizability (10^{-36} esu) in the static case.

	γ_{xxxx}	γ_{yyyy}	γ_{zzzz}	γ_{xxyy}	γ_{yyzz}	γ_{xxzz}	$\langle\gamma\rangle$
Isolated	26.11	17.87	181.26	4.91	9.69	36.86	65.63
Embedded	25.10	18.92	194.08	4.98	9.81	38.64	68.99
Δ%	3.87	5.88	7.07	1.43	1.24	4.83	5.12

https://doi.org/10.1371/journal.pone.0175859.t007

the tensor representing the first hyperpolarizability, since in general the influence of an electrostatic field is great. One example is the signal change that occurs for the $\boldsymbol{\beta}_{xxx}$ and $\boldsymbol{\beta}_{xyy}$ components, as also reported in earlier studies [36,38].

The dynamic effects of the linear polarizability, the first hyperpolarizability, and the second hyperpolarizability are shown in. The second average hyperpolarizability γ(-2ω;ω,ω,0) is a dc-electric field induced second harmonic generation (EFISH), while the value γ(-ω;ω,0,0) corresponds to the Kerr effect. The linear polarizability α(-ω;ω), the first hyperpolarizability $\beta_{||}$(-2ω;ω,ω), and the second average hyperpolarizability γ(-2ω;ω,ω,0), for the isolated and embedded FBHZ at frequency ω = 0.042 au, are shown in Table 8. Comparing the value of the α(-ω;ω) and γ(-2ω;ω,ω,0) at frequency ω = 0.0428 au, for the isolated FBHZ in the static cases α(0;0) and γ(0;0,0,0), we note an increase of 3.31% and 44.64%, respectively. When we compare the values of the crystal FBHZ at frequency ω = 0.0428 au of α(-ω;ω) and γ(-2ω;ω,ω,0) in the static cases α(0;0) and γ(0;0,0,0), we have an increase of 3% and 47% respectively. The first hyperpolarizability $\beta_{||}$(-2ω;ω,ω) at frequency ω = 0.042 a.u. of the crystal FBHZ shows an increase of 17.20% when compared with the isolated FBHZ.

The dispersion curves of the linear polarizability and the first and second hyperpolarizabilities for the isolated and embedded FBHZ molecules are shown in (Fig 10). The linear polarizabilities of the embedded and isolated molecules of FBHZ show a similar behaviour as a function of the frequency of an external applied field, the same being true for the first and second hyperpolarizabilities.

Table 9 shows the influence of polarization upon the electron density of the FBHZ due to the field of point charges of the atoms of neighbouring molecules, which can also be qualitatively analysed in terms of the partial atomic charges. The results of the CHELPG charges for the isolated and embedded cases show a small charge transfer between C–H···F (C12 –H12···F1). This occurs due to a weak hydrogen bond. Within the dihedral angles of the crystal, the fragment that transfers the greatest charge between the isolated FBHZ and the embedded FBHZ is (*C5–O2–C8–C9*). One reason for the small γ growth and, to a lesser degree, μ and $\boldsymbol{\beta}$ in a crystalline environment can be found in the results shown in Table 9. There is a significant charge transfer from ring B (C5-C6-C7-C2-C3-C4) around 41.64%; the conformation (C8-O2) received the greatest charge, around 38.35%.

We also used an implicit solvation scheme, based on PCM integral equation formalism (PCM-IEF). In this case, calculations of the dynamic electrical properties of FBHZ were implemented, but this time including different solvents (Gas-Phase, Acetone, Chloroform,

Table 8. CAM-B3LYP/6-311+G(d) results for the dynamic linear polarizability (10^{-24} esu), first hyperpolarizability (10^{-30} esu), and second hyperpolarizability (10^{-36} esu) of the isolated and embedded FBHZ at frequency ω = 0.0428 a.u.

FBHZ	α(-ω;ω)	β||(-2ω;ω,ω)	γ(-2ω;ω,ω,0)
Isolated	39.50	9.77	94.93
Embedded	39.65	11.45	101.56
Δ%	0.38	17,20	7,00

https://doi.org/10.1371/journal.pone.0175859.t008

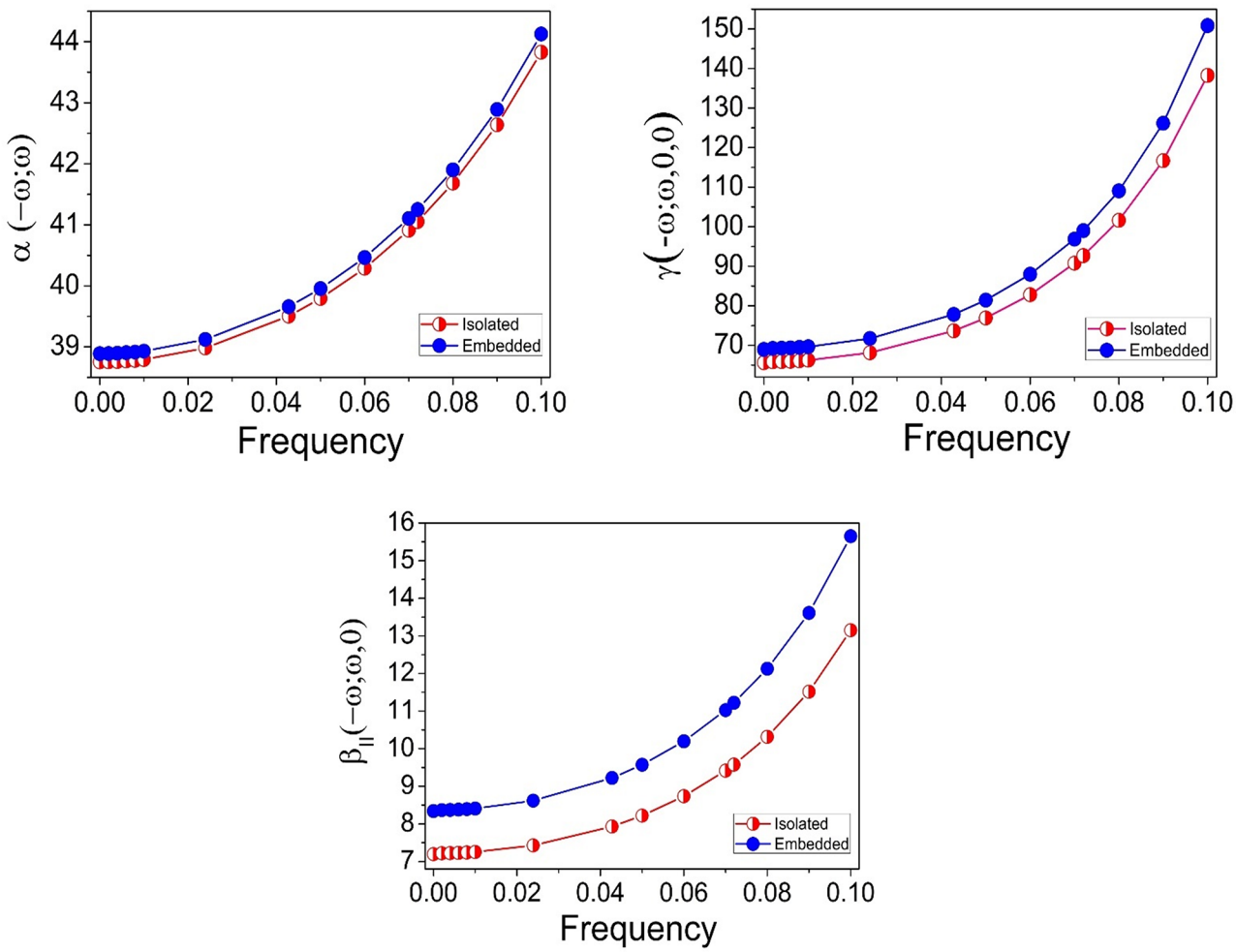

Fig 10. Dynamic evolution of the calculated values for the linear polarizability (10^{-24} esu), first hyperpolarizability (10^{-30} esu), and second hyperpolarizability (10^{-36} esu) of FBHZ with the respective number of frequencies.

https://doi.org/10.1371/journal.pone.0175859.g010

Dichloromethane, Dimethyl sulfoxide, Ethanol, Methanol, and Water). The results can be seen in S6 Table. For the extreme cases, i.e., the gas-phase and dimethyl sulfoxide (DMSO), the linear polarizability and the first and second hyperpolarizability are shown in Table 10. As in the case discussed in Table 8, the values γ(-2ω;ω,ω,0), $\beta_{||}$(-2ω;ω,ω) and α(-ω,ω) are much more sensitive in the presence of solvents. We can numerically confirm that DMSO increased the value of γ(-2ω;ω,ω,0) by nearly 62.65%, whereas for β||(-2ω;ω,ω) and α(-ω;ω), the increase was 71.93% and 10.82%, respectively.

Frontier molecular orbitals

The orbital of a molecule can be ordered according to either the energy levels in a diagram, which can be mounted, or the experimental results using computational methods (theoretical calculation). The molecular orbital of highest energy, occupied by at least one electron, is called the *HOMO*, and the molecular orbital of lowest energy not occupied by electrons, the *LUMO* [88,89]. The values of the energy of the HOMO and LUMO for the isolated molecule are −7.74 *eV*, 1.89 *eV* respectively. In accordance with these energies, we can calculate the chemical potential, hardness and electronegativity. The energy difference between HOMO and LUMO

Table 9. MP2/6-311+G d results for the CHELPG atomic charges of isolated and embedded FBHZ.

Number	Atom	Charge ($10^{-19}C$)		
		Isolated	Converged	Δ%
1	N2	-0.41	-0.42	2.44
2	O2	-0.75	-0.95	26.67
3	O1	-0.88	-1.01	14.77
4	N1	-0.50	-0.58	16.00
5	H1	0.42	0.49	16.67
6	C5	0.66	0.83	25.76
7	C4	-0.45	-0.48	6.67
8	H4	0.25	0.28	12.00
9	C3	-0.06	-0.05	16.67
10	H3	0.18	0.20	11.11
11	C7	-0.21	-0.21	0.00
12	H7	0.22	0.24	9.09
13	C1	1.02	1.11	8.82
14	C2	-0.23	-0.31	34.78
15	C6	-0.36	-0.44	22.22
16	H6	0.23	0.25	8.70
17	C16	-0.10	-0.17	70.00
18	C15	0.36	0.37	2.78
19	H15	0.12	0.17	41.67
20	C9	0.06	0.13	116.67
21	C19	-0.16	-0.13	18.75
22	H19	0.17	0.18	5.88
23	C17	-0.18	-0.18	0.00
24	H17	0.15	0.14	6.67
25	C8	0.69	0.68	1.45
26	H8A	-0.06	0.02	133.33
27	H8B	-0.10	-0.06	40.00
28	C21	-0.08	-0.07	12.50
29	H21	0.11	0.13	18.18
30	C10	-0.56	-0.55	1.79
31	H10	0.31	0.34	9.68
32	C11	0.73	0.70	4.11
33	C18	-0.11	-0.15	36.36
34	H18	0.16	0.16	0.00
35	C14	-0.31	-0.38	22.58
36	H14	0.23	0.24	4.35
37	C13	-0.09	-0.12	33.33
38	H13	0.18	0.19	5.56
39	F1	-0.47	-0.46	2.13
40	C20	-0.15	-0.17	13.33
41	H20	0.17	0.20	17.65
42	C12	-0.45	-0.44	2.22
43	H12	0.28	0.28	0.00

https://doi.org/10.1371/journal.pone.0175859.t009

Table 10. CAM-B3LYP/6-311+G(d) results for the dynamic linear polarizability (10^{-24} esu), first hyperpolarizability (10^{-30} esu) and second hyperpolarizability (10^{-36} esu) of gas-phase and DMSO solvent FBHZ for the frequency ω = 0.0428 a.u.

Medium	α(-ω;ω)	β||(-2ω;ω,ω)	γ(-2ω;ω,ω,0)
Gas-Phase	43.62	9.19	129.38
DMSO	48.34	15.80	210.44
Δ%	10.82	71.93	62.65

https://doi.org/10.1371/journal.pone.0175859.t010

(*Band* − *Gap*) was calculated for both isolated and embedded FBHZ: the following values were found: 9.63 *eV* and 9.39 *eV*. The *Band* − *Gap* is an indicator of molecular stability; compounds with a high *Band* − *Gap* are stable [90,91].

The first hyperpolarizability can also be connected to the band gap of energy between the *HOMO* and *LUMO*. So, the higher the *Band* − *Gap* is, the lower the first hyperpolarizability. When we compare the value of the Band-Gap of the isolated molecule with that of the embedded molecule, we note a percentage decrease of 2.5%, which indicates that the embedded molecule has a higher potential for applications in NLO [91].

Looking at the energy Band-Gap between the *HOMO* and *LUMO* of the molecule FBHZ in a solvent medium, in this case DMSO see (Fig 11) and Gas-Phase see (Fig 12), we note a small Band-Gap of 6.97 eV (DMSO) and 7.03 eV (Gas-Phase), which indicates that crystal FBHZ has promising applications for NLO. The energy Band-Gap between the HOMO and LUMO for different solvents (Acetone, Chloroform, Dichloromethane, Ethanol, Methanol, and Water) can be seen in S8–S13 Figs.

In the results for the gas-phase FBHZ, the oscillator strength of the second state is much weaker compared to the first state, see Table 11. When the calculation is done in DMSO, the weaker state is the second excited state. The transitions reported show that the states change places when going from gas-phase to DMSO and the transition from HOMO to LUMO becomes lower in energy than the transition from HOMO to LUMO+1 in the DMSO system.

Conclusions

In this work we have determined the total dipole moment, the linear polarizability and the first and second hyperpolarizabilities of the FBHZ crystal. We employed a supermolecule approach combined with an iterative scheme of electrostatic polarization, where the atoms of neighbouring molecules are represented by point charges. This technique can represent the experimental results very successfully, see Ref. [36,38]. Urea is a prototypical molecule used in the NLO properties of molecular systems. Hence, it was used frequently as a threshold value for the purpose of comparison[92]. Thus we have found that the total dipole moment of the FBHZ embedded molecule is approximately 3.18 times greater than that of Urea while the total first order hyperpolarizability is 40.6 times greater than that of Urea and the second hyperpolarizability is 16.6 times greater than that of Urea. The result of the calculation of first hyperpolarizability of the crystal FBHZ is 40% greater than the experimental result for the (1E,4E)-1,5-di-p-tolylpenta-1,4-dien-3-one[84]. Hence, we can conclude, on the basis of the magnitude of the first order hyperpolarizability of the FBHZ, that it offers potential applications in the development of NLO material. Our results for NLO properties are of the same order of magnitude ($\chi^{(3)} \approx 10^{-19}\ m^2/V^2\ (SI)$) of other crystals found in the literature, e.g., bulk gold[85,86]. This demonstrates that FBHZ constitutes a promising object for future studies and applications in NLO and quantum dots[87]. The dynamic electrical properties of FBHZ in different solvent media are also reported. For example, the values of γ(-2ω;ω,ω,0) increased almost 62.65%,

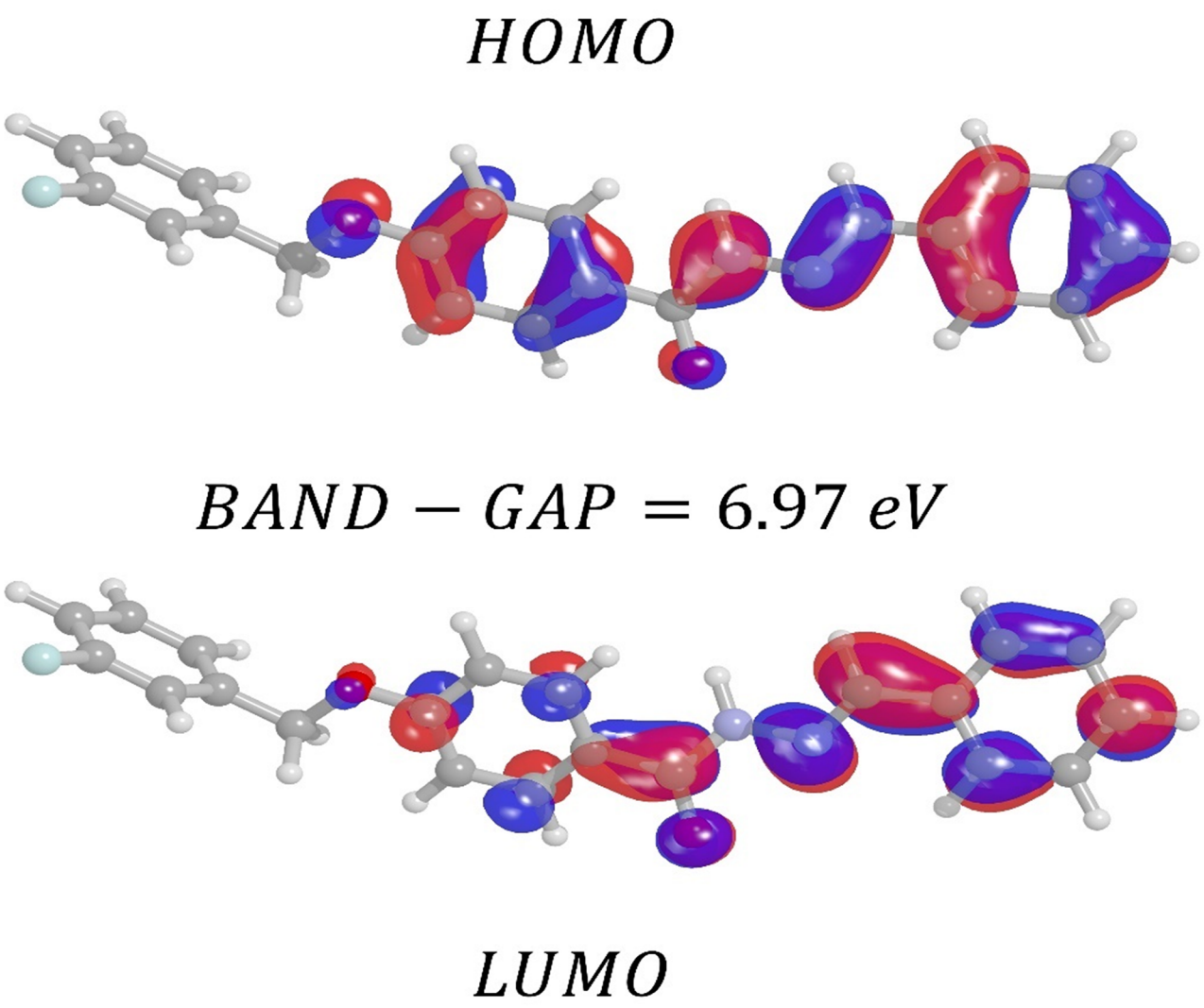

Fig 11. Molecular orbital plots, showing HOMO-LUMO as obtained in the CAM-B3LYP/6-311+G(d) level of theory for DMSO solvent, for the FBHZ molecule.

https://doi.org/10.1371/journal.pone.0175859.g011

while for values $\beta_{||}(-2\omega;\omega,\omega)$ and $\alpha(-\omega,\omega)$ the increases were 71.93% and 10.82%, respectively, compared to the solvent-free situation.

The results for ChelpG charges show that the weak hydrogen bond causes little charge transfer between C–H···F.

The d_{norm} surfaces (HS) corroborate previously discussed information about weak hydrogen bonds, but the C–H···F was an exception, as it was not clearly observed, even demonstrating $d_{C12\cdots F1}$ 3.477(6) Å and $\angle_{C12-H12\cdots F1}$ 141.45(3°. However, through the 2D fingerprint plot this contact rises to contribute 9.9%. The DSC/TGA and Hot-stage Microscopy analysis were performed, and the results show the crystal's stability in relation to temperature variation.

We hope that the interesting dynamic physical properties displayed by this organic crystal can motivate researchers who are involved in modern photonic devices to explore its potential more thoroughly.

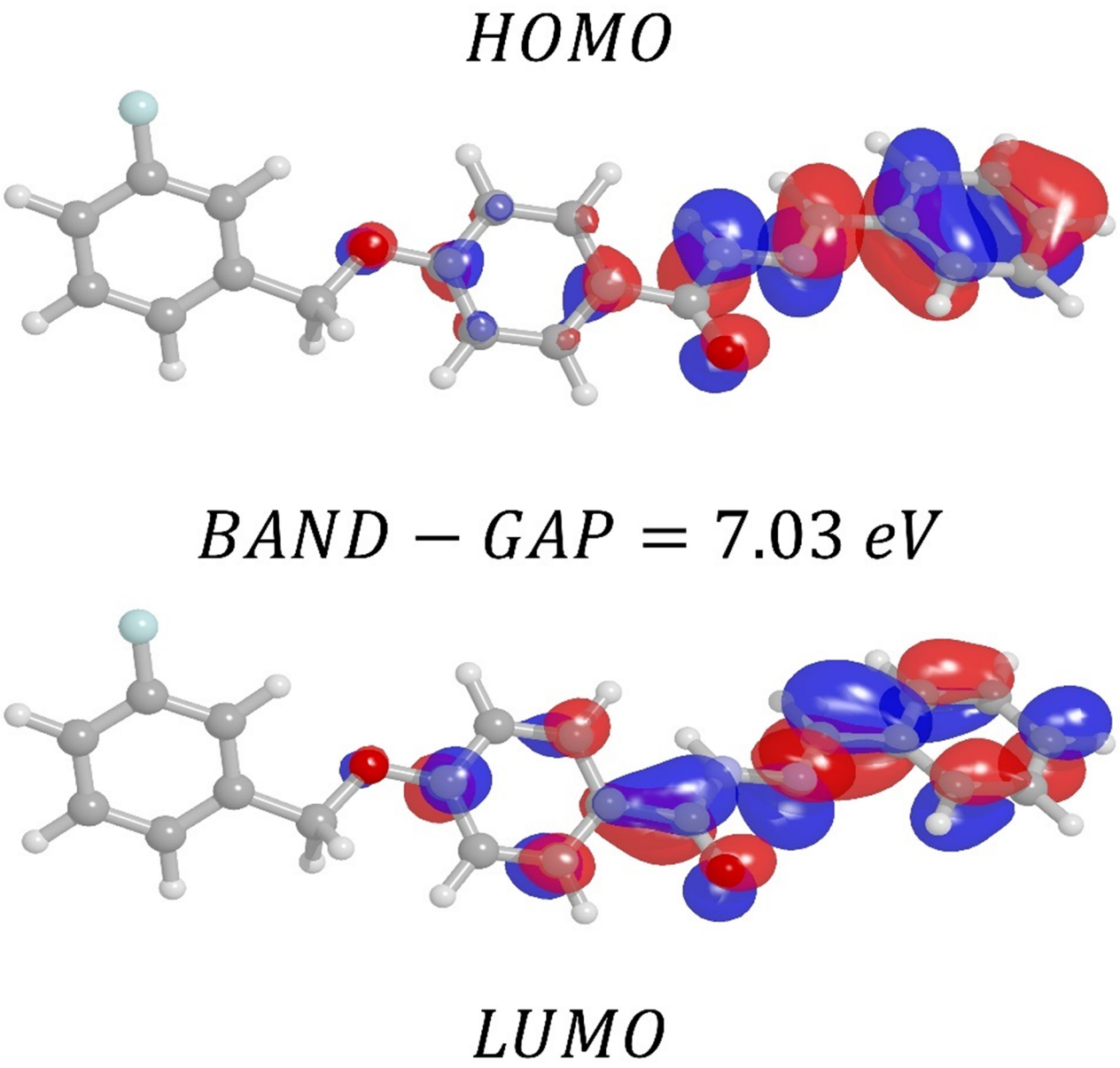

Fig 12. Molecular orbital plots, showing HOMO-LUMO as obtained in the CAM-B3LYP/6-311+G(d) level of theory for gas-phase, for the FBHZ molecule.

https://doi.org/10.1371/journal.pone.0175859.g012

Table 11. TDDFT PBE1PBE/6-311+G(2d,p) of the FBHZ molecule in the gas phase and DMSO.

	Wavelength (nm)	Energy (eV)	Oscillator Strength
Gas-Phase			
State 1	442.39	2.8026	0.0148
State 2	393.43	3.1513	0.0004
DMSO			
State 1	402.24	3.0824	1.4014
State 2	297.91	4.1618	0.1696

https://doi.org/10.1371/journal.pone.0175859.t011

Supporting information

S1 Fig. Synthesis and characterization.
(TIF)

S2 Fig. Infrared spectrum of FBHZ (4000–400 cm-1).
(TIF)

S3 Fig. Mass spectrum of FBHZ.
(TIF)

S4 Fig. 1H NMR spectrum (1-dimensional) of FBHZ (DMSO-d6, 500 MHz) plotted as signal intensity vs. chemical shift (ppm) and the expanded region (range 7.0–12 ppm) (DMSO-d6, 500MHz).
(TIF)

S5 Fig. 13C NMR spectrum (1-dimensional) of FBHZ plotted as signal intensity vs. chemical shift (ppm) (DMSO-d6, 500 MHz).
(TIF)

S6 Fig. UV scan spectrum of FBHZ showing the baseline of ethanol 99% and the wavelength (λ) of maximum absorbance.
(TIF)

S7 Fig. The unit cell of FBHZ.
(TIF)

S8 Fig. Molecular orbital plots, showing HOMO-LUMO as obtained in the CAM-B3LYP/6-311+G(d) level of theory for Acetone solvent, for the FBHZ molecule.
(TIF)

S9 Fig. Molecular orbital plots, showing HOMO-LUMO as obtained in the CAM-B3LYP/6-311+G(d) level of theory for Chloroform solvent, for the FBHZ molecule.
(TIF)

S10 Fig. Molecular orbital plots, showing HOMO-LUMO as obtained in the CAM-B3LYP/6-311+G(d) level of theory for Dichloromethane solvent, for the FBHZ molecule.
(TIF)

S11 Fig. Molecular orbital plots, showing HOMO-LUMO as obtained in the CAM-B3LYP/6-311+G(d) level of theory for Ethanol solvent, for the FBHZ molecule.
(TIF)

S12 Fig. Molecular orbital plots, showing HOMO-LUMO as obtained in the CAM-B3LYP/6-311+G(d) level of theory for Methanol solvent, for the FBHZ molecule.
(TIF)

S13 Fig. Molecular orbital plots, showing HOMO-LUMO as obtained in the CAM-B3LYP/6-311+G(d) level of theory for Water solvent, for the FBHZ molecule.
(TIF)

S1 Table. Crystal data and structure refinement of FBHZ.
(DOCX)

S2 Table. Fractional atomic coordinates (×104) and equivalent isotropic displacement parameters (Å2×103) for FBHZ. Ueq is defined as 1/3 of of the trace of the orthogonalised

UIJ tensor.
(DOCX)

S3 Table. Anisotropic displacement parameters (Å2×103) for FBHZ. The Anisotropic displacement factor exponent takes the form: -2π2[h2a*2U11+2hka*b*U12+. . .].
(DOCX)

S4 Table. Bond lengths and angles between bonds for FBHZ.
(DOCX)

S5 Table. Hydrogen atom coordinates (Å×104) and isotropic displacement parameters (Å2×103) for FBHZ.
(DOCX)

S6 Table. CAM-B3LYP/6-311+G(d) results for the dynamic linear polarizability (10–24 esu), first hyperpolarizability (10–30 esu) and second hyperpolarizability (10–36 esu) of various solvent FBHZ for the frequency ω = 0.0428 a.u.
(DOCX)

Acknowledgments

The authors would like to thank the following Brazilian agencies for financial support: Conselho Nacional de Desenvolvimento Científico e Tecnológico (CNPq), Coordenação de Aperfeiçoamento Pessoal de Nível Superior (CAPES) and Fundação de Apoio à Pesquisa do Estado de Goiás (FAPEG).

Author Contributions

Conceptualization: GLBA CV HBN BB.

Data curation: GLBA CV HBN BB.

Formal analysis: GLBA CV HBN BB.

Investigation: GLBA CV HBN BB.

Methodology: GLBA CV HBN BB.

Resources: GLBA CV HBN BB.

Software: GLBA CV HBN BB.

Supervision: PSC GLBA CV HBN BB.

Validation: GLBA CV HBN BB.

Visualization: GLBA CV HBN BB.

Writing – original draft: RFNR LRA FGS PSC WCS KSM GLBA CV HBN BB.

References

1. Picón-Ferrer I, Hueso-Ureña F, Illán-Cabeza NA, Jiménez-Pulido SB, Martínez-Martos JM, Ramírez-Expósito MJ, et al. Chloro-fac-tricarbonylrhenium(I) complexes of asymmetric azines derived from 6-acetyl-1,3,7-trimethylpteridine-2,4(1H,3H)-dione with hydrazine and aromatic aldehydes: preparation, structural characterization and biological activity against several human t. J Inorg Biochem. 2009; 103: 94–100. https://doi.org/10.1016/j.jinorgbio.2008.09.014 PMID: 19019451

2. Zhao X, Wang X-Z, Jiang X-K, Chen Y-Q, Li Z-T, Chen G-J. Hydrazide-Based Quadruply Hydrogen-Bonded Heterodimers. Structure, Assembling Selectivity, and Supramolecular Substitution. J Am Chem Soc. American Chemical Society; 2003; 125: 15128–15139.
3. Sugiura M, Kobayashi S. N-acylhydrazones as versatile electrophiles for the synthesis of nitrogen-containing compounds. Angew Chem Int Ed Engl. 2005; 44: 5176–86. https://doi.org/10.1002/anie.200500691 PMID: 16059954
4. Licandro E, Perdicchia D. N-Acylhydrazines: Future Perspectives Offered by New Syntheses and Chemistry. European J Org Chem. 2004; 2004: 665–675.
5. Zhang B, Zhao Y, Zhai X, Wang L, Yang J, Tan Z, et al. Design, Synthesis and Anticancer Activities of Diaryl Urea Derivatives Bearing N-Acylhydrazone Moiety. Chem Pharm Bull. 2012; 60: 1046–1054. PMID: 22863709
6. do Amaral DN, Cavalcanti BC, Bezerra DP, Ferreira PMP, Castro R de P, Sabino JR, et al. Docking, Synthesis and Antiproliferative Activity of N-Acylhydrazone Derivatives Designed as Combretastatin A4 Analogues. Afarinkia K, editor. PLoS One. 2014; 9: e85380. https://doi.org/10.1371/journal.pone.0085380 PMID: 24614859
7. Rodrigues DA, Ferreira-Silva GÀ, Ferreira ACS, Fernandes RA, Kwee JK, Sant'Anna CMR, et al. Design, Synthesis, and Pharmacological Evaluation of Novel N -Acylhydrazone Derivatives as Potent Histone Deacetylase 6/8 Dual Inhibitors. J Med Chem. 2016; 59: 655–670. https://doi.org/10.1021/acs.jmedchem.5b01525 PMID: 26705137
8. Carcelli M, Rogolino D, Gatti A, De Luca L, Sechi M, Kumar G, et al. N-acylhydrazone inhibitors of influenza virus PA endonuclease with versatile metal binding modes. Sci Rep. 2016; 6: 31500. https://doi.org/10.1038/srep31500 PMID: 27510745
9. Silva AG, Zapata-Sudo G, Kummerle AE, Fraga CAM, Barreiro EJ, Sudo RT. Synthesis and vasodilatory activity of new N-acylhydrazone derivatives, designed as LASSBio-294 analogues. Bioorg Med Chem. 2005; 13: 3431–3437. https://doi.org/10.1016/j.bmc.2005.03.003 PMID: 15848755
10. Bamba M, Imamoğlu A, Carusotto I, Ciuti C. Origin of strong photon antibunching in weakly nonlinear photonic molecules. Phys Rev A—At Mol Opt Phys. 2011; 83: 1–4.
11. Ferretti S, Savona V, Gerace D. Optimal antibunching in passive photonic devices based on coupled nonlinear resonators. New J Phys. 2013; 15: 25012.
12. Gerace D, Savona V. Unconventional photon blockade in doubly resonant microcavities with second-order nonlinearity. Phys Rev A. 2014; 89: 31803.
13. Irvine WTM, Hennessy K, Bouwmeester D. Strong Coupling between Single Photons in Semiconductor Microcavities. Phys Rev Lett. 2006; 96: 57405.
14. Shen HZ, Zhou YH, Yi XX. Quantum optical diode with semiconductor microcavities. Phys Rev A. 2014; 90: 23849.
15. Shen HZ, Zhou YH, Yi XX. Tunable photon blockade in coupled semiconductor cavities. Phys Rev A. 2015; 91: 63808.
16. Xu X-W, Li Y. Strong photon antibunching of symmetric and antisymmetric modes in weakly nonlinear photonic molecules. Phys Rev A. 2014; 90: 33809.
17. Xu X-W, Li Y-J. Antibunching photons in a cavity coupled to an optomechanical system. J Phys B At Mol Opt Phys. 2013; 46: 35502.
18. Zhang W, Yu Z, Liu Y, Peng Y. Optimal photon antibunching in a quantum-dot–bimodal-cavity system. Phys Rev A. 2014; 89: 43832.
19. Zhou YH, Shen HZ, Yi XX. Unconventional photon blockade with second-order nonlinearity. Phys Rev A. 2015; 92: 23838.
20. Mukhopadhyay S, Risko C, Marder SR, Brédas J-L, Bredas JL, Adant C, et al. Polymethine dyes for all-optical switching applications: a quantum-chemical characterization of counter-ion and aggregation effects on the third-order nonlinear optical response. Chem Sci. The Royal Society of Chemistry; 2012; 3: 3103.
21. Karthigha S, Kalainathan S, Hamada F, Yamada M, Kondo Y, Ruiz B, et al. Synthesis, growth and third-order nonlinear optical properties of quinolinium single crystal-PCLQI. RSC Adv. The Royal Society of Chemistry; 2016; 6: 33159–33169.
22. Narayanan S, Raghunathan SP, Poulose AC, Mathew S, Sreekumar K, Sudha Kartha C, et al. Third-order nonlinear optical properties of 3,4-ethylenedioxythiophene copolymers with chalcogenadiazole acceptors. New J Chem. The Royal Society of Chemistry; 2015; 39: 2795–2806.
23. Johnson JC, Li Z, Ndione PF, Zhu K, Mitzi DB, Feild CA, et al. Third-order nonlinear optical properties of methylammonium lead halide perovskite films. J Mater Chem C. The Royal Society of Chemistry; 2016; 4: 4847–4852.

24. Wang D, Guo Q, Gao H, Yang Z, Xing Y, Cao H, et al. The application of double click to synthesize a third-order nonlinear polymer containing donor–acceptor chromophores. Polym Chem. The Royal Society of Chemistry; 2016; 7: 3714–3721.
25. Sun Z, Chen T, Cai N, Chen J, Li L, Wang Y, et al. Synthesis, growth and characterization of a third-order nonlinear optical crystal based on the borate ester with sodium supporting its structural framework. New J Chem. The Royal Society of Chemistry; 2011; 35: 2804.
26. Lian Z, Jiang K, Lou T, He GS, Tan L, Zhang Q, et al. Structures and third-order nonlinear optical properties of two three-dimensional Cd (ii) coordination polymers with trinodal (3, 4, 5) and dinodal (4, 5) connected network topologies. RSC Adv. The Royal Society of Chemistry; 2015; 5: 82781–82788.
27. Zhang X, Luo W, Wang L-J, Jiang W. Third-order nonlinear optical vitreous material derived from mesoporous silica incorporated with Au nanoparticles. J Mater Chem C. The Royal Society of Chemistry; 2014; 2: 6966.
28. Feng Q, Li Y, Shi G, Wang L, Zhang W, Li K, et al. A photo-controllable third-order nonlinear optical (NLO) switch based on a rhodamine B salicylaldehyde hydrazone metal complex. J Mater Chem C. The Royal Society of Chemistry; 2016; 327: 1485–1488.
29. Champagne B, Bishop DM. Calculations of Nonlinear Optical Properties for the Solid State. Advances in Chemical Physics. Hoboken, NJ, USA: John Wiley & Sons, Inc.; 2003. pp. 41–92.
30. ZYSS J, CHEMLA DS. Quadratic Nonlinear Optics and Optimization of the Second-Order Nonlinear Optical Response of Molecular Crystals. Nonlinear Optical Properties of Organic Molecules and Crystals. 1st ed. New York: Elsevier; 1987. pp. 23–191.
31. Xu X-W, Li Y. Tunable photon statistics in weakly nonlinear photonic molecules. Phys Rev A. 2014; 90: 43822.
32. Kanis DR, Ratner MA, Marks TJ. Design and construction of molecular assemblies with large second-order optical nonlinearities. Quantum chemical aspects. Chem Rev. American Chemical Society; 1994; 94: 195–242.
33. Karakas a., El kouari Y, Migalska- Zalas A, Sahraoui B. Ab-initio calculations on static and dynamic third-order optical nonlinearity of azo-azulenes. Photonics Lett Pol. 2012; 4: 17–19.
34. KARAKAŞ A, KOÇ ZE, FRIDRICHOVÁ M, NĚMEC P, KROUPA J. THE INVESTIGATION OF SECOND-ORDER NONLINEAR OPTICAL PROPERTIES OF P-NITROPHENYLAZOANILINE: SECOND HARMONIC GENERATION AND AB INITIO COMPUTATIONS. J Theor Comput Chem. World Scientific Publishing Company; 2012; 11: 209–221.
35. Georg HC, Coutinho K, Canuto S. Converged electronic polarization of acetone in liquid water and the role in the n–π* transition. Chem Phys Lett. 2006; 429: 119–123.
36. Fonseca TL, Sabino JR, Castro MA, Georg HC. A theoretical investigation of electric properties of L-arginine phosphate monohydrate including environment polarization effects. J Chem Phys. 2010; 133: 1–8.
37. Castro AN, Almeida LR, Anjos MM, Oliveira GR, Napolitano HB, Valverde C, et al. Theoretical study on the third-order nonlinear optical properties and structural characterization of 3-Acetyl-6-Bromocoumarin. Chem Phys Lett. Elsevier B.V.; 2016; 653: 122–130.
38. Santos OL, Fonseca TL, Sabino JR, Georg HC, Castro MA. Polarization effects on the electric properties of urea and thiourea molecules in solid phase. J Chem Phys. 2015; 143: 234503. https://doi.org/10.1063/1.4937481 PMID: 26696062
39. Seidler T, Champagne B. Which charge definition for describing the crystal polarizing field and the χ (1) and χ (2) of organic crystals? Phys Chem Chem Phys. 2015; 17: 19546–19556. https://doi.org/10.1039/c5cp03248b PMID: 26144533
40. Seidler T, Stadnicka K, Champagne B. Evaluation of the linear and second-order NLO properties of molecular crystals within the local field theory: Electron correlation effects, choice of XC functional, ZPVA contributions, and impact of the geometry in the case of 2-methyl-4-nitroaniline. J Chem Theory Comput. 2014; 10: 2114–2124. https://doi.org/10.1021/ct5001654 PMID: 26580538
41. Seidler T, Stadnicka K, Champagne B. Second-order Nonlinear Optical Susceptibilities and Refractive Indices of Organic Crystals from a Multiscale Numerical Simulation Approach. Adv Opt Mater. 2014; 2: 1000–1006.
42. Seidler T, Stadnicka K, Champagne B. Investigation of the linear and second-order nonlinear optical properties of molecular crystals within the local field theory. J Chem Phys. 2013; 139: 114105. https://doi.org/10.1063/1.4819769 PMID: 24070277
43. Seidler T, Stadnicka K, Champagne B. Linear and second-order nonlinear optical properties of ionic organic crystals. J Chem Phys. 2014; 141: 104109. https://doi.org/10.1063/1.4894483 PMID: 25217906
44. Bruker. APEX2. Bruker AXS Inc., Madison, Wisconsin, USA.; 2007.

45. Bruker. SAINT. Bruker AXS Inc., Madison, Wisconsin, USA.; 2007.
46. Sheldrick GM. A short history of SHELX. Acta Crystallogr Sect A. 2008; 64: 112–122.
47. Sheldrick GM. Crystal structure refinement with SHELXL. Acta Crystallogr Sect C. 2015; 71: 3–8.
48. Dolomanov OV, Bourhis LJ, Gildea RJ, Howard JAK, Puschmann H. OLEX2: a complete structure solution, refinement and analysis program. J Appl Crystallogr. 2009; 42: 339–341.
49. Farrugia LJ. WinGX and ORTEP for Windows: an update. J Appl Crystallogr. 2012; 45: 849–854.
50. Macrae CF, Edgington PR, McCabe P, Pidcock E, Shields GP, Taylor R, et al. Mercury: visualization and analysis of crystal structures. J Appl Crystallogr. 2006; 39: 453–457.
51. Macrae CF, Bruno IJ, Chisholm JA, Edgington PR, McCabe P, Pidcock E, et al. Mercury CSD 2.0—new features for the visualization and investigation of crystal structures. J Appl Crystallogr. 2008; 41: 466–470.
52. Gavezzotti A, Filippini G. Geometry of the Intermolecular X-H.cntdot..cntdot..cntdot.Y (X, Y = N, O) Hydrogen Bond and the Calibration of Empirical Hydrogen-Bond Potentials. J Phys Chem. American Chemical Society; 1994; 98: 4831–4837.
53. Gavezzotti A. Are Crystal Structures Predictable? Acc Chem Res. American Chemical Society; 1994; 27: 309–314.
54. Nardelli M. PARST95—an update to PARST: a system of Fortran routines for calculating molecular structure parameters from the results of crystal structure analyses. J Appl Crystallogr. 1995; 28: 659.
55. Desiraju GR. Crystal engineering: from molecule to crystal. J Am Chem Soc. American Chemical Society; 2013; 135: 9952–67.
56. Desiraju GR, Steiner T. The Weak Hydrogen Bond: In Structural Chemistry and Biology. Oxford University Press; 2001.
57. Desiraju GR. A bond by any other name. Angew Chem Int Ed Engl. 2011; 50: 52–9. https://doi.org/10.1002/anie.201002960 PMID: 21031379
58. Tiekink ERT, Zukerman-Schpector J. The Importance of Pi-Interactions in Crystal Engineering [Internet]. Tiekink ERT, Zukerman-Schpector J, editors. Chichester, UK: John Wiley & Sons, Ltd; 2012.
59. Desiraju GR, Vittal JJ, Ramanan A. Crystal Engineering. Crystal Engineering. Co-Published with Indian Institute of Science (IISc), Bangalore, India; 2011. pp. 1–23.
60. Allen FH. The Cambridge Structural Database: a quarter of a million crystal structures and rising. Acta Crystallogr Sect B. 2002; 58: 380–388.
61. Wolff SK, Grimwood DJ, McKinnon JJ, Turner MJ, Jayatilaka D, Spackman MA. CrystalExplorer (Version 3.1). University of Western Australia; 2012.
62. Jayatilaka D, Wolff SK, Grimwood DJ, McKinnon JJ, Spackman MA. CrystalExplorer: a tool for displaying Hirshfeld surfaces and visualising intermolecular interactions in molecular crystals. Acta Crystallogr Sect A. International Union of Crystallography; 2006; 62: s90.
63. Jayatilaka D, Grimwood DJ, McKinnon JJ, Lee A, Lemay A, Russel AJ, et al. TONTO—A System for Computational Chemistry. 2005.
64. Jayatilaka D, Grimwood DJ. Computational Science—ICCS 2003: International Conference, Melbourne, Australia and St. Petersburg, Russia, June 2–4, 2003 Proceedings, Part IV. In: Sloot PMA, Abramson D, Bogdanov A V, Gorbachev YE, Dongarra JJ, Zomaya AY, editors. Berlin, Heidelberg: Springer Berlin Heidelberg; 2003. pp. 142–151.
65. Batsanov SS. Van der Waals Radii of Elements. Inorg Mater. 2001; 37: 871–885.
66. Bondi A. van der Waals Volumes and Radii. J Phys Chem. American Chemical Society; 1964; 68: 441–451.
67. Guillaume M, Champagne B, Bégué D, Pouchan C. Electrostatic interaction schemes for evaluating the polarizability of silicon clusters. J Chem Phys. 2009; 130: 134715. https://doi.org/10.1063/1.3104629 PMID: 19355772
68. Kanoun MB, Botek E, Champagne B. Electrostatic modeling of the linear optical susceptibilities of 2-methyl-4-nitroaniline, m-nitroaniline, 3-methyl-4-nitropyridine N-oxide and 2-carboxylic acid-4-nitropyridine-1-oxide crystals. Chem Phys Lett. 2010; 487: 256–262.
69. Kongsted J, Osted A, Mikkelsen K V, Christiansen O. Second harmonic generation second hyperpolarizability of water calculated using the combined coupled cluster dielectric continuum or different molecular mechanics methods. J Chem Phys. 2004; 120: 3787–98. https://doi.org/10.1063/1.1642593 PMID: 15268543
70. Gavezzotti A. The Crystal Packing of Organic Molecules: Challenge and Fascination Below 1000 Da. Crystallogr Rev. 1998; 7: 5–121.
71. Gavezzotti A. Are Crystal Structures Predictable? Acc Chem Res. 1994; 27: 309–314.

72. Wolstenholme DJ, Cameron TS. Comparative Study of Weak Interactions in Molecular Crystals: H−H Bonds vs Hydrogen Bonds†. J Phys Chem A. American Chemical Society; 2006; 110: 8970–8978.
73. Takahashi O, Kohno Y, Nishio M. Relevance of weak hydrogen bonds in the conformation of organic compounds and bioconjugates: evidence from recent experimental data and high-level ab initio MO calculations. Chem Rev. American Chemical Society; 2010; 110: 6049–76.
74. Calhorda MJ. Weak hydrogen bonds: theoretical studies. Chem Commun. The Royal Society of Chemistry; 2000; 801–809.
75. Lee KM, Chang H-C, Jiang J-C, Lu L-C, Hsiao C-J, Lee Y-T, et al. Probing C-H. . .X hydrogen bonds in amide-functionalized imidazolium salts under high pressure. J Chem Phys. 2004; 120: 8645–50. https://doi.org/10.1063/1.1697380 PMID: 15267793
76. Nishio M, Umezawa Y, Honda K, Tsuboyama S, Suezawa H. CH/π hydrogen bonds in organic and organometallic chemistry. CrystEngComm. The Royal Society of Chemistry; 2009; 11: 1757.
77. Kryachko E, Scheiner S. CH· · ·F Hydrogen Bonds. Dimers of Fluoromethanes. J Phys Chem A. American Chemical Society; 2004; 108: 2527–2535.
78. Spada L, Gou Q, Vallejo-Lopez M, Lesarri A, Cocinero EJ, Caminati W. Weak C-H[three dots, centered]N and C-H[three dots, centered]F hydrogen bonds and internal rotation in pyridine-CH3F. Phys Chem Chem Phys. The Royal Society of Chemistry; 2014; 16: 2149–2153.
79. Rohde D, Yan C-J, Wan L-J. C−H· · ·F Hydrogen Bonding: The Origin of the Self-Assemblies of Bis(2,2'-difluoro-1,3,2-dioxaborine). Langmuir. American Chemical Society; 2006; 22: 4750–4757.
80. Schonleber A, van Smaalen S, Weiss H-C, Kesel AJ. N-H. . .O and C-H. . .F hydrogen bonds in the incommensurately modulated crystal structure of adamantan-1-ammonium 4-fluorobenzoate. Acta Crystallogr Sect B. International Union of Crystallography; 2014; 70: 652–659.
81. Espinosa E, Lecomte C, Molins E, Veintemillas S, Cousson A, Paulus W. Electron density study of a new non-linear optical material: L-arginine phosphate monohydrate (LAP). Comparison between X–X and X–(X + N) refinements. Acta Crystallogr Sect B Struct Sci. 1996; 52: 519–534.
82. Spackman MA, Munshi P, Dittrich B. Dipole Moment Enhancement in Molecular Crystals from X-ray Diffraction Data. ChemPhysChem. 2007; 8: 2051–2063. https://doi.org/10.1002/cphc.200700339 PMID: 17676648
83. Spackman MA, Munshi P, Jayatilaka D. The use of dipole lattice sums to estimate electric fields and dipole moment enhancement in molecular crystals. Chem Phys Lett. 2007; 443: 87–91.
84. Aditya Prasad A, Muthu K, Meenatchi V, Rajasekar M, Agilandeshwari R, Meena K, et al. Optical, vibrational, NBO, first-order molecular hyperpolarizability and Hirshfeld surface analysis of a nonlinear optical chalcone. Spectrochim Acta Part A Mol Biomol Spectrosc. 2015; 140: 311–327.
85. Sámson ZL, Horak P, MacDonald KF, Zheludev NI. Femtosecond surface plasmon pulse propagation. Opt Lett. 2011; 36: 250. https://doi.org/10.1364/OL.36.000250 PMID: 21263516
86. Boyd RW, Shi Z, De Leon I. The third-order nonlinear optical susceptibility of gold. Opt Commun. 2014; 326: 74–79.
87. Seo J, Ma S, Yang Q, Creekmore L, Battle R, Brown H, et al. Large Resonant Third-order Optical Nonlinearity of CdSe Nanocrystal Quantum Dots. J Phys Conf Ser. 2006; 38: 91–94.
88. De Proft F, Sablon N, Tozer DJ, Geerlings P. Calculation of negative electron affinity and aqueous anion hardness using kohn-Sham HOMO and LUMO energies. Faraday Discuss. 2007; 135: 151–159 259, 503–506. PMID: 17328427
89. Hagberg DP, Marinado T, Karlsson KM, Nonomura K, Qin P, Boschloo G, et al. Tuning the HOMO and LUMO Energy Levels of Organic Chromophores for Dye Sensitized Solar Cells. J Org Chem. 2007; 72: 9550–9556. https://doi.org/10.1021/jo701592x PMID: 17979286
90. Zhang G, Musgrave CB. Comparison of DFT methods for molecular orbital eigenvalue calculations. J Phys Chem A. 2007; 111: 1554–1561. https://doi.org/10.1021/jp061633o PMID: 17279730
91. Arshad MN, Bibi A, Mahmood T, Asiri AM, Ayub K. Synthesis, crystal structures and spectroscopic properties of triazine-based hydrazone derivatives; a comparative experimental-theoretical study. Molecules. 2015; 20: 5851–5874. https://doi.org/10.3390/molecules20045851 PMID: 25854752
92. Prashanth J, Ramesh G, Naik JL, Ojha JK, Reddy BV, Rao GR. Molecular Structure, Vibrational Analysis and First Order Hyperpolarizability of 4-Methyl-3-Nitrobenzoic Acid Using Density Functional Theory. Opt Photonics J. 2015; 5: 91–107.